Petroleum Science 22 (2025) 5142–5165

Contents lists available at ScienceDirect

Petroleum Science

journal homepage: www.keaipublishing.com/en/journals/petroleum-science

Original Paper

Real-time NMR experimental study of displacement–imbibition coupling in tight/shale oil reservoirs: Lithological variations, influencing factors, and key insights

Bin-Yu Wang [a,b], Ren-Yi Cao [a,*], Xin-Yi Zheng [a], Lin-Song Cheng [a], Jiang-Peng Hu [a], Zhi-Hao Jia [a], Wen-Hao Duan [c], Hassan Hassanzadeh [b]

[a] College of Petroleum Engineering, China University of Petroleum (Beijing), Beijing, 102249, China
[b] Department of Chemical & Petroleum Engineering, Schulich School of Engineering, University of Calgary, Calgary, Alberta, T2N 1N4, Canada
[c] PetroChina Changqing Oilfield Company, Xi'an, 710000, Shaanxi, China

ARTICLE INFO

Article history:
Received 5 January 2025
Received in revised form
20 August 2025
Accepted 20 August 2025
Available online 27 August 2025

Edited by Yan-Hua Sun

Keywords:
Displacement–imbibition coupling mechanisms
Matrix and fracture
Lithologies
Nuclear magnetic resonance (NMR) experiment
Tight/shale oil reservoir
Pore scale

ABSTRACT

Displacement–imbibition coupling production is a pivotal technology for enhancing oil recovery (EOR) in waterflooded tight/shale oil reservoirs. However, the microscopic fluid transport mechanisms across different pore scales remain inadequately understood. This study presents an innovative real-time nuclear magnetic resonance (NMR) experimental system integrated with MRI-based image processing to dynamically monitor oil–water distribution and quantify local oil saturation during injection–shut-in–production. This approach enables quantitative evaluation of pore utilization across different pore size ranges and reveals the impacts of various driving forces on oil displacement efficiency. The results show that displacement–imbibition coupling production employs multiple mechanisms to achieve balanced contributions from pores of all size scales. The displacement–imbibition oil production mainly consists of three stages: displacement-dominated injection, capillary-driven imbibition during shut-in, and displacement–imbibition coupling effects during production. Pressure oscillations significantly enhance matrix–fracture exchange by lowering pore-throat entry thresholds and redistributing pressure fields. Quantitative analysis shows that large pore dominate early displacement, while small pore contribute more during imbibition. Lithology and pore-throat connectivity critically influence displacement efficiency; vitric tuff outperforms argillaceous siltstone by up to 11.8%. Notably, greater fracture complexity increases the oil–water contact area, enhancing capillary imbibition, reducing reliance on displacement forces, and increasing the contribution of displacement–imbibition coupling effects to oil displacement efficiency by 15.35%. Artificially modifying the pressure field to induce pressure oscillations, effectively utilizing the high conductivity of fractures, and fully leveraging the displacement–imbibition coupling effects within matrix pores are crucial for achieving optimal EOR. Lastly, a new concept of nonlinear flow zoning is introduced to describe spatial variations in flow behavior under complex coupling conditions. These experimentally validated insights into matrix–fracture interactions provide theoretical support for designing improved waterflooding strategies and optimizing oil recovery in tight and shale reservoirs.

1. Introduction

With the rapid depletion of conventional resources and the steady growth of global energy consumption, unconventional oil and gas resources have attracted widespread attention (EIA, 2022; Syed et al., 2022; Tian et al., 2023). The shale oil reservoirs in China are predominantly of continental depositional origin, and the micro- to nano-scale pore-throat structures vary significantly

* Corresponding author.
E-mail address: caorenyi@126.com (R.-Y. Cao).

Peer review under the responsibility of China University of Petroleum (Beijing).

https://doi.org/10.1016/j.petsci.2025.08.028
1995-8226/

across different lithologies even within the same region (Lei et al., 2022; Zhang Q. et al., 2023). These reservoirs are characterized by low porosity and low permeability, fine pore-throat, poor connectivity, and strong heterogeneity. In addition, the development of multi-scale natural fractures differs widely, often preventing effective displacement (Cai et al., 2022; Jia et al., 2023; Jin et al., 2021; Zou et al., 2023). In recent years, the combination of hydraulic fracturing and water injection in horizontal wells has enabled the initial effective utilization of shale oil (Jiang et al., 2024; Lu et al., 2024; Sheng and Chen, 2014; Zhang et al., 2024). However, the significant permeability contrast between the matrix and fractures often causes the injected water to flow preferentially through fractures, resulting in water channeling, making the water injection ineffective (Lei et al., 2024; Lv et al., 2019). As a result, substantial volumes of residual oil remain trapped in the reservoir matrix. This challenge highlights the urgent need for advanced and efficient development methods, bringing increasing attention to displacement–imbibition coupling oil production technology. Considering different lithologies (varying pore-throat structures) and the coupling between matrix and fractures, effectively leveraging the displacement–imbibition coupling/synergistic effect between the matrix and fractures is critical for the efficient development of tight and shale oil.

Compared to gas injection methods, water-based EOR techniques have garnered significant attention from researchers due to their lower cost and reduced risk of gas channeling (Han et al., 2024; Jiang et al., 2019; Qu et al., 2021; Song et al., 2024; Wu et al., 2019). Among these, imbibition has been widely recognized as a key mechanism in improving recovery during water injection (Fu et al., 2024; Ghandi et al., 2019; Guo et al., 2021; Li et al., 2023; Lin et al., 2016; Zhang et al., 2022). Imbibition can be generally classified as either spontaneous or forced (displacement). In tight and shale reservoirs, the water injection development process primarily involves displacement–imbibition (forced imbibition). This mechanism builds upon spontaneous imbibition by incorporating the effect of injection pressure entering the matrix or fractures. In such low-permeability systems, displacement–imbibition coupling arises from the interaction of viscous, capillary, and pressure-induced forces during the injection–shut-in–production process. This coupling generates pressure oscillations within the pore network, facilitating the utilization of residual oil that would otherwise remain unrecovered by conventional waterflooding (Li et al., 2018; Peng et al., 2024). However, this dynamic process is not uniform and is highly sensitive to reservoir conditions such as lithology, fracture geometry, pore structure, and wettability (Harimi et al., 2019; Kerunwa et al., 2016; Vilhena et al., 2019; Zhang and Yang, 2024). These factors significantly influence the effectiveness of the displacement–imbibition coupling production and the EOR effect. Although the significance of imbibition has been demonstrated in many studies, the mechanisms underlying displacement–imbibition coupling across different lithologies and flow stages remain insufficiently characterized. In particular, the interplay between matrix and fracture domains and their respective contributions to recovery during each production stage (injection, shut-in, production) lack systematic investigation. Clarifying the multiscale, multiphase flow behavior is essential for optimizing recovery strategies in tight and shale reservoirs.

Extensive experimental investigations have been carried out to explore imbibition mechanisms in various lithologies such as tuff, sandstone, and shale (Meng et al., 2022; Ren et al., 2023; Yu et al., 2021). These studies primarily rely on core-scale physical experiments to assess the driving factors behind oil recovery enhancement through imbibition. For instance, Takahashi and Kovscek (2010) focusing on Barnett and Bakken shales, demonstrated that modifying capillary pressure and interfacial tension significantly influences recovery efficiency. Dou et al. (2021) evaluated spontaneous and forced imbibition effects in tight sandstone, revealing how pore size distribution affects displacement efficiency under different injection strategies. Similarly, Yang et al. (2016) conducted a comparative study of sandstone, tuff, and shale cores, showing that imbibition performance is closely linked to pore-throat structure, clay content, and connectivity. Other researchers have quantitatively linked imbibition displacement efficiency with reservoir quality index, maximum connected pore-throat radius, and overall pore network connectivity (Wei et al., 2016; Xiong et al., 2025). These studies collectively highlight that lithological variability plays a dominant role in controlling fluid behavior during capillary-driven flow. However, most of the above work has focused on spontaneous imbibition in isolation, often within a single lithology or a simplified pore system. Few studies have examined displacement–imbibition coupling under realistic development scenarios that involve fracture–matrix interaction, especially during the injection–shut-in–production process. Moreover, the influence of lithological heterogeneity on coupling behavior, particularly the contributions of different pore size classes across flow stages, remains poorly understood. This gap underscores the need for systematic experimental studies integrating real-time monitoring and quantitative characterization to fully elucidate the role of lithology and fractures in displacement–imbibition coupling mechanisms.

Core-scale flooding experiments remain one of the most effective methods for simulating displacement and imbibition behavior in porous and fractured reservoir media. In recent years, nuclear magnetic resonance (NMR) and magnetic resonance imaging (MRI) have emerged as powerful non-invasive tools for capturing oil and water distribution within cores of varying pore-throat structures (Cheng et al., 2015; Jiang et al., 2023; Liu et al., 2024; Wang et al., 2020; Xu et al., 2020). These technologies enable spatial visualization and quantitative evaluation of two-phase fluid flow and have significantly advanced our understanding of multiphase transport in tight and shale reservoirs. A number of studies have leveraged these tools to explore specific influencing factors. For example, Dai et al. (2019) examined the roles of injection rate, interfacial tension, imbibition time, and permeability on oil recovery in heterogeneous pore networks. Du et al. (2024) integrated fractal theory with NMR data to characterize saturation profiles and identify key controls on displacement efficiency in shale cores. Wang et al. (2024) focused on the impact of fracture morphology on coupled displacement–imbibition mass transfer, emphasizing the dynamic interplay between matrix and complex fracture systems during the injection–shut-in–production process. While these efforts have significantly deepened the understanding of flow behavior, most current studies are confined to optimizing injection parameters or isolated conditions, and few have systematically addressed the underlying mechanisms of displacement–imbibition coupling across diverse lithologies. Furthermore, there remains a lack of quantitative frameworks that integrate imaging-based saturation tracking with physical oil production measurements. In particular, little attention has been paid to the relative contributions of different pore size classes and driving forces throughout each production stage. Therefore, there is a pressing need for integrated experimental approaches that can not only visualize displacement–imbibition dynamics but also quantitatively link pore-scale saturation evolution with macroscopic recovery efficiency under varying lithological and fracture conditions.

In summary, there are three main issues currently: (1) There is a lack of research on the displacement–imbibition coupling mechanism between the matrix and fractures in tight/shale oil reservoirs. (2) The influence of different lithologies on the displacement–imbibition coupling mechanism and flow patterns has been ignored. (3) Quantitative and visualized characterization of the displacement–imbibition effects and microscopic migration patterns across different pore sizes throughout the entire injection–shut-in–production process is lacking. Addressing these challenges, this study focuses on the displacement–imbibition coupling mechanisms in oil recovery across different lithologies and the real-time oil and water distribution. An experimental method for displacement–imbibition using real-time NMR/MRI technology is developed, and multiple sets of NMR experiments are conducted. The study separately examined the effects of different injection strategies, different lithologies, and differing levels of fracture complexity on oil displacement efficiency and oil saturation field maps. Additionally, it conducts a detailed investigation into the microscopic migration behavior of fluids within the pores under the displacement–imbibition coupling effects. Simultaneously, we develop a novel method combining MRI and image processing to characterize oil saturation, enabling the investigation of oil saturation variations in different pore regions during the displacement–imbibition coupling process. This approach facilitates the quantitative evaluation of the contribution of displacement–imbibition coupling effects. This work aims to explore the various factors on displacement–imbibition coupling effects, analyze the microscopic migration behavior of crude oil between matrix pores and fractures, and provide theoretical support for the efficient utilization of tight/shale oil reservoirs.

2. Physical experiment

2.1. Experimental apparatus, materials, and design

2.1.1. Apparatus

To optimize oil–water two-phase displacement–imbibition experiments, we developed a real-time displacement–imbibition NMR system (Fig. 1). This system integrates real-time NMR technology with a core displacement apparatus, which is based on the experimental platform of the Reservoir Numerical Simulation Group (RNSG) at China University of Petroleum (Beijing). The main apparatus primarily includes an NMR device (Mac-roMR12-150H-I, Niumai, Suzhou, China), an adjustable-length ceramic core holder (Tuochuang Co., Ltd., 0–60 MPa, 0–70 °C), and a high-temperature and high-pressure circulation system (21060, Tuochuang Co., Ltd., Jiangsu, China). The drive system and the data acquisition and analysis system are each connected to the main apparatus. The drive system primarily consists of an ISCO pump (Teledyne ISCO, Lincoln, NE, USA), an air compressor (OTS-500), and two 500 mL intermediate containers (Tuochuang Co., Ltd., 50 MPa). The data acquisition and analysis system can directly observe the changes within the core, allowing for continuous monitoring of the displacement–imbibition coupling process and enhancing the accuracy of experimental results. In addition, in order to eliminate the effects of the equipment itself, the parameters are calibrated before each experiment using standard samples provided by the equipment manufacturer, thus keeping the initial parameters (RF amplitude and RF pulse width) consistent.

2.1.2. Materials

The cores used in the experiment include argillaceous siltstone samples from the Lucaogou Formation in the Jimsar Depression of the Junggar Basin, argillaceous tuff samples from the Lucaogou Formation in the Malang Depression of the Santanghu Basin, and vitric tuff samples from the Lucaogou Formation in the Niujuanhu area of the Santanghu Basin. According to conventional lithological analysis, the porosity of the Lucaogou Formation ranges between 2% and 10%, with permeability values between 0.001 and 0.1mD, characterizing it as a typical low-porosity, low-permeability tight shale reservoir. The mineral composition, primary storage spaces, and pore-fracture types of different lithological cores can be determined through X-ray diffraction (XRD) whole-rock mineral content analysis (Table 1) and focused ion beam scanning electron microscopy (FIB-SEM) experiments, providing critical support for the analysis of subsequent experimental results. Based on the mineral content analysis, the reservoirs in the Junggar east area are primarily composed of feldspar (mainly plagioclase, with relatively less K-feldspar) and quartz, with a high content of calcite and dolomite, while clay mineral content is relatively low. In the Niujuanhu area, the reservoir minerals predominantly consist of quartz and feldspar, accounting for 70%–98%, with minor amounts of calcite and dolomite, trace amounts of zeolite, and little to no clay minerals. In the Santanghu area, clay mineral content is also low, averaging less than 5%, whereas felsic minerals and dolomite are more abundant, with a combined average exceeding 90%. The scan results reveal two primary types of reservoir spaces: matrix pores and fractures. Matrix pores are further classified into five types: intragrain pores, intergranular pores, intercrystalline pores, dissolution pores, and organic pores. Fractures are categorized into two main types: inorganic and organic fractures. The argillaceous siltstone primarily contains dissolution micropores and residual intergranular pores, with locally developed dissolution structural fractures (Fig. 2(a)–(c)). The argillaceous tuff and vitric tuff mainly develop intergranular and intragranular pores, dissolution pores, intercrystalline pores, and fractures (Fig. 2(d)–(f)). However, vitric tuff exhibits a high degree of fracture development (Fig. 2(j)), reaching a density of 33 fractures per meter, with good pore connectivity. Thus, considering the mineral composition, pore types, and fracture development, the reservoir in the Niujuanhu area of the Santanghu Basin is classified as a tight oil reservoir. The fracture development in the argillaceous tuff is relatively low (Fig. 2(k)), with only 10 fractures per meter, and the argillaceous siltstone exhibits almost no fractures (Fig. 2(l)). Therefore, the reservoirs in the Jimsar Depression of the Junggar Basin and the Malang Depression of the Santanghu Basin are categorized as shale oil reservoirs.

Additionally, based on FIB-SEM scanning results, we use Avizo software to process data from different lithological cores, further clarifying the influence of lithology and fractures on fluid flow. The scanned results of different lithologies are subjected to threshold segmentation, identifying and filtering fine pore-throat and fractures to construct pore-throat models, followed by velocity field simulations under unidirectional flow conditions. As shown in Fig. 3(a)–(c), the pore-throat connectivity in vitric tuff and argillaceous tuff is relatively high. However, due to the presence of numerous natural fractures and microfractures, vitric tuff exhibits a wider pore distribution, allowing fluid to flow more easily through its pore-throat system, forming multiple dominant streamlines (Fig. 3(e)). In contrast, argillaceous tuff has a lower pore-throat connectivity and fewer fractures, resulting in fewer and less extensive streamlines compared to vitric tuff (Fig. 3(f)). Argillaceous siltstone, on the other hand, is characterized by dense pores and narrow throats, significantly restricting fluid flow. Conventional displacement methods struggle to establish effective flow channels within its pore system, making it the least favorable for flow, as shown in Fig. 3(d). Therefore, lithology, along with the complex structure of matrix pores and fractures, significantly influences the effectiveness of displacement–imbibition coupling effects, ultimately impacting oil displacement efficiency.

2.1.3. Design

To examine how various injection strategies, lithologies, and fracture complexities influence displacement–imbibition coupling

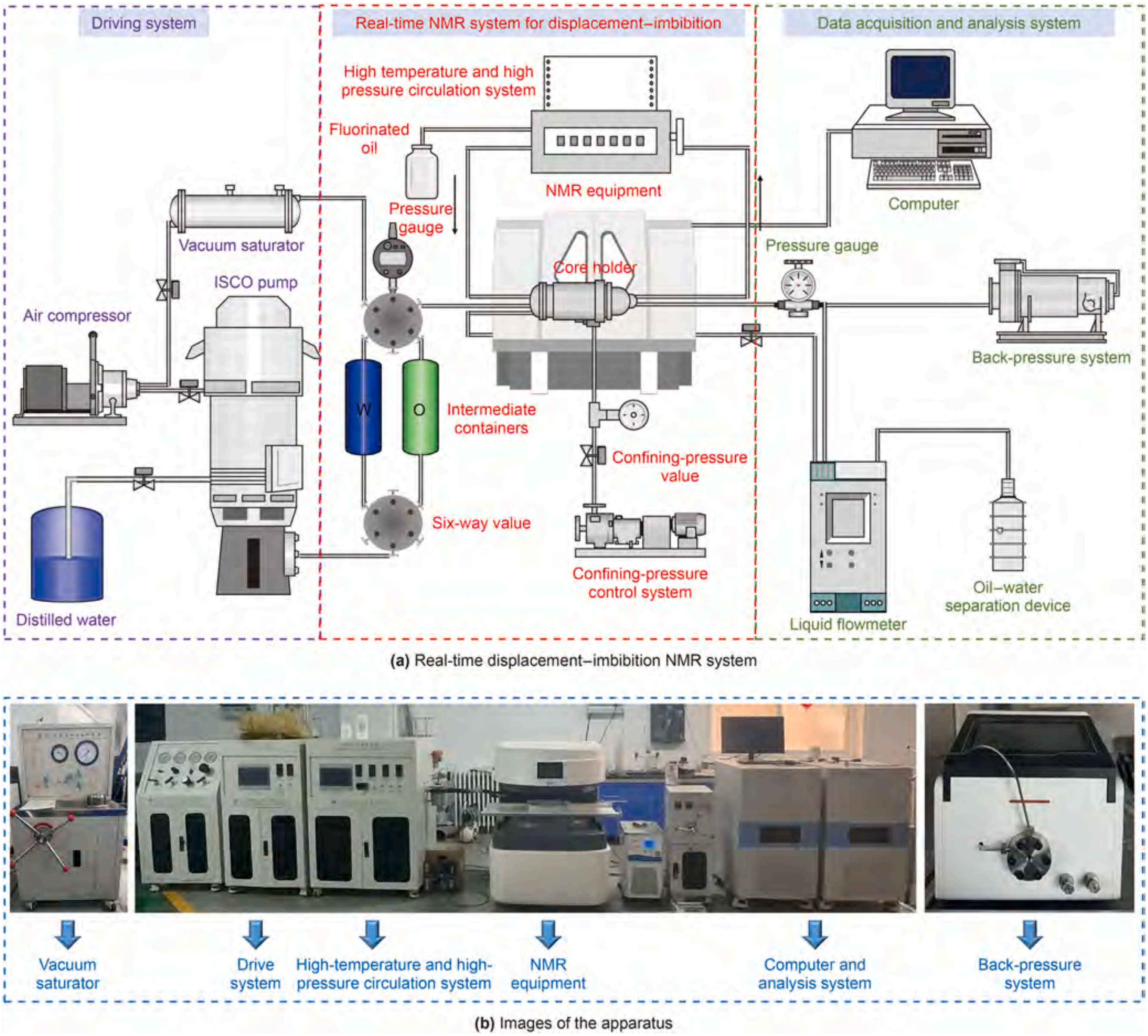

Fig. 1. Schematic diagram of real-time displacement–imbibition NMR system.

Table 1
X-ray diffraction (XRD) whole-rock mineral content analysis results of the target reservoirs.

Lithology	Depth, m	Mineral content, %								
		Quartz	K-feldspar	Plagioclase	Calcite	Siderite	Pyrite	Anhydrite	Dolomite	Total clay
Argillaceous siltstone	3987.72	24.2	7.6	24.4	5.9	1.5	0.3	1.4	29.4	5.3
Vitric tuff	2250.16	57.2	0	34.6	4.8	–	–	–	1.4	2.0
Argillaceous tuff	2493.02	29.6	5.4	3.8	1.2	–	0.4	–	49.2	10.4

effects, we prepared 13 core samples, each measuring 2.5 cm in diameter and 5 cm in length, by sectioning full-sized cores sourced from different locations. The sample details are listed in Table 2 and the specific core preparation process is shown in Fig. 4. Before the experiments, core samples C1–C9 were treated with artificial fractures at both ends, with fracture lengths set to one-fourth of the core length. For each core from the same area, three injection strategies—continuous injection, water huff and puff, and displacement–imbibition coupling production are considered to simulate the effects of varying injection strategies and lithologies. To study the impact of fracture complexity on displacement–imbibition coupling effects, further treatments are applied to cores from the Santanghu area. Core samples C10 and C11 are fractured at half and three-quarters of the core length, respectively, to simulate varying fracture penetration ratios. Core sample C12, naturally containing a throughgoing fracture, and core sample C13, which naturally exhibits developed fractures, are used to evaluate the effects of varying fracture development. The

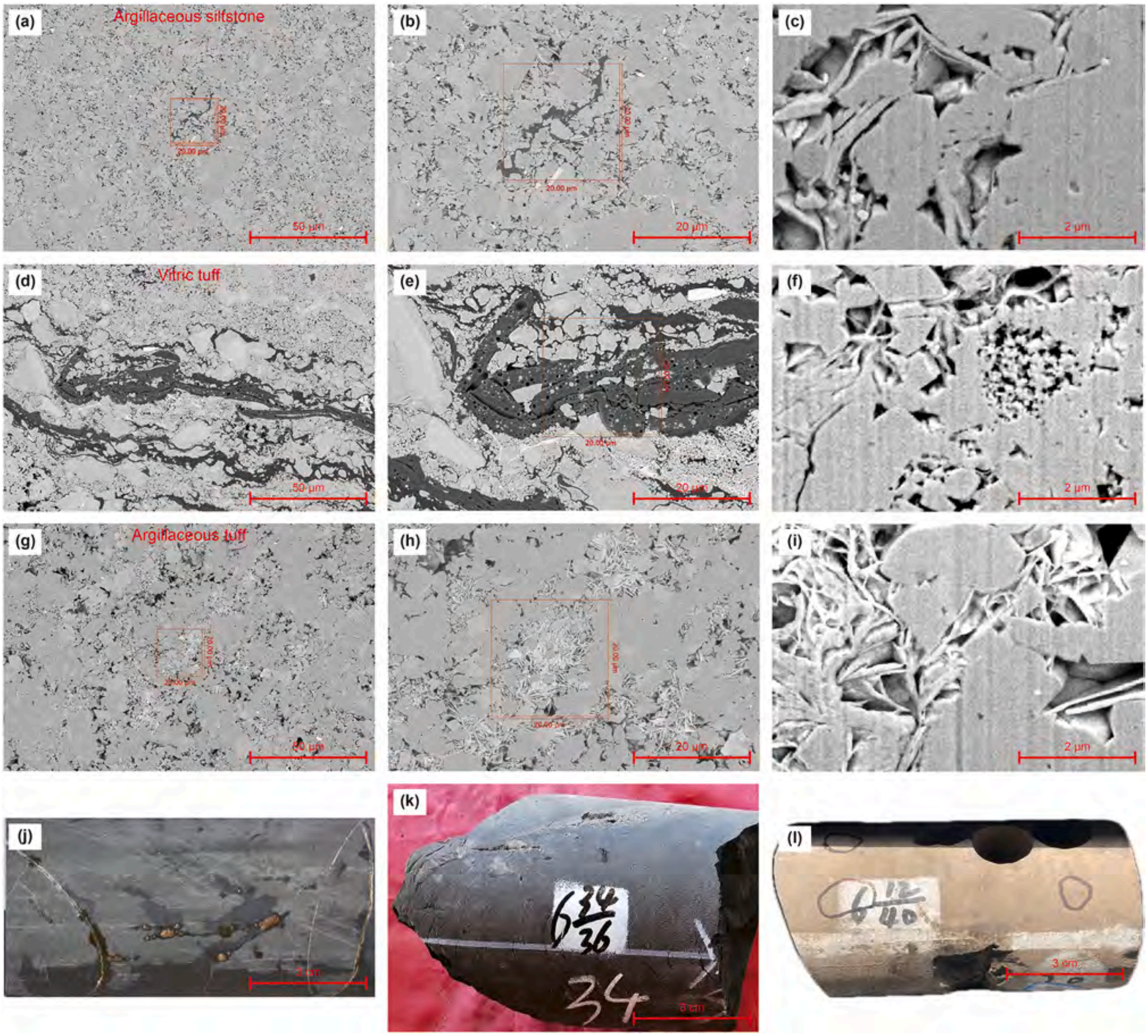

Fig. 2. Microscopic pore-throat characteristics of cores from different areas, full-size core display.

complete experimental design is shown in Table 3. Additionally, to simulate oil–water flow under actual reservoir conditions, oil samples are extracted from reservoirs in the Junggar east, Santanghu, and Niujuanhu areas. The viscosity and density of these oils at 25 °C and 10 MPa are 4.2 mPa s and 0.876 g/cm^3 for the Junggar east sample, 16.65 mPa s and 0.829 g/cm^3 for the Santanghu sample, and 6.59 mPa s and 0.800 g/cm^3 for the Niujuanhu sample. The water sample used in experiments is deuterium oxide. Its viscosity and density at 25 °C and 10 MPa are 1.023 mPa s and 1.107 g/cm^3.

2.2. Experimental procedure

The experimental procedure consists of four main stages: basic preparation, core preparation, core saturation, and core displacement. The detailed experimental steps are outlined as follows.

(1) Basic preparations: The materials for the experiment, such as the oil sample, water sample, core, etc., are prepared in accordance with the experimental designs, and the central device is connected and its airtightness is verified.
(2) Core preparation: For samples C1–C9, a wire-cutting device is used to create fractures in the central sections at both ends of the cores, with each cut length measuring 1.25 cm, or 1/4 of the core length, and 5 mm in width. Quartz sand (120 mesh) is then packed into these artificial fractures and fixed in place with epoxy resin. Excess quartz sand is brushed away to ensure smooth inlet and outlet surfaces. For samples C10 and C11, similar cutting is performed, but the total fracture lengths are adjusted to 1/2 and 3/4 of the core length, respectively. Finally, for samples C12 and C13, the existing fractures are only filled with quartz sand and secured with epoxy resin to maintain smooth inlet and outlet surfaces without additional fracture creation at the ends.
(3) Core saturation: The prepared cores are washed with oil, dried, and weighed. Next, they are placed in a vacuum saturator and vacuumed for 24 h using an air compressor. The cores are then pressurized to 25 MPa, and the

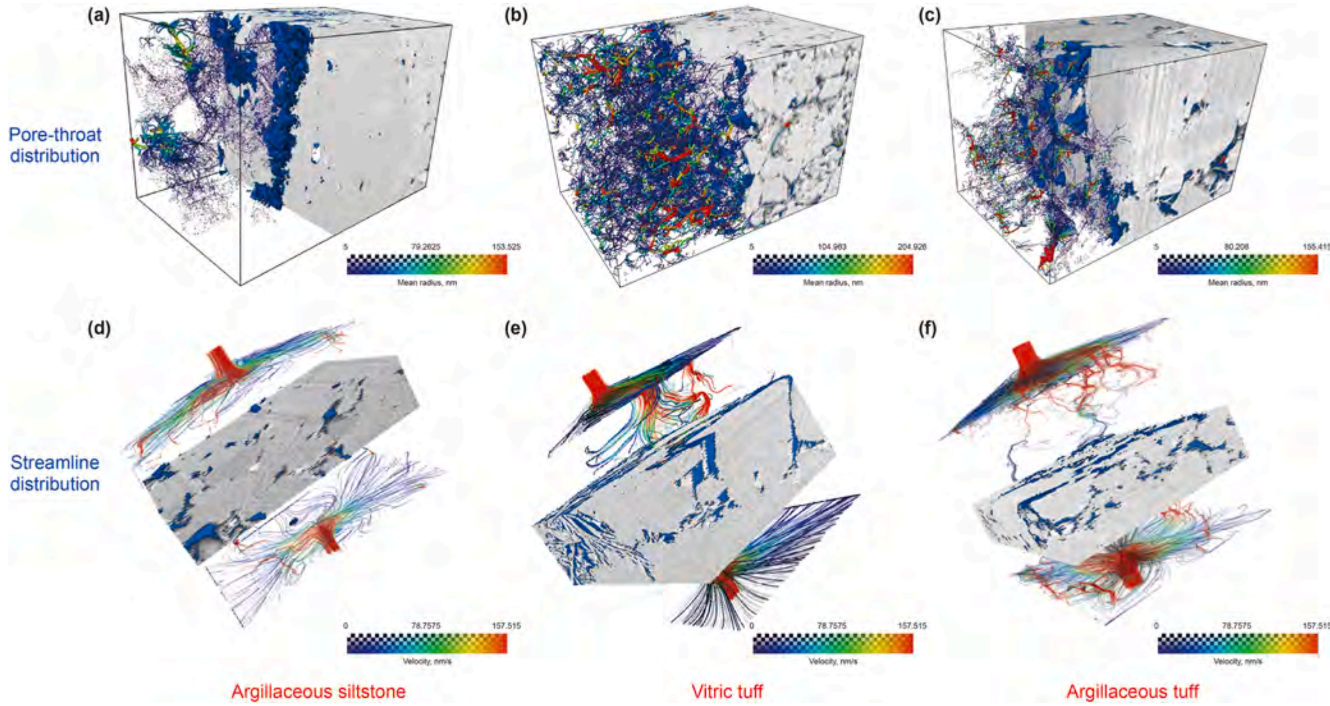

Fig. 3. Pore-throat distribution at different lithological pore scales and unidirectional flow streamline distribution diagram.

Table 2
Basic core parameters for the experiment.

Core sample No.	Diameter, cm	Length, cm	Porosity, %	Air permeability, mD	Estimated water permeability, mD	Lithology
C1	2.440	5.003	2.7	0.001	0.00006	Argillaceous siltstone (Junggar east area)
C2	2.438	4.991	2.8	0.005	0.00031	
C3	2.441	3.567	3.1	0.009	0.00054	
C4	2.445	4.943	3.3	0.063	0.00378	Vitric tuff (Niujuanhu area)
C5	2.438	4.985	3.5	0.183	0.01099	
C6	2.434	4.987	5.2	0.217	0.01303	
C7	2.442	4.981	2.8	0.003	0.00018	Argillaceous tuff (Santanghu area)
C8	2.444	4.986	3.2	0.006	0.00036	
C9	2.438	4.987	3.4	0.017	0.00102	
C10	2.440	4.979	3.3	0.015	0.00090	
C11	2.436	4.980	3.2	0.022	0.00132	
C12	2.442	4.998	3.4	0.026	0.00156	
C13	2.440	5.003	4.3	0.053	0.00318	

experimental oil is used to saturate them by pressure difference through the inlet valve. It takes five days to ensure that all the gas in the pores of the cores is discharged. After saturation, the wet weight of the cores is measured. The cores are then placed into the core holder, and the temperature is set to 50 °C. Besides, the Q-CPMG sequence is used to collect the core pore-throat signal at a resonance frequency of 12 MHz and an echo time (TE) of 0.5 ms, a digital gain setting of 5, an analog gain setting of 15, a preamplifier setting of 3, an accumulation number of 16 (to ensure the signal-to-noise ratio and scanning accuracy), a waiting time setting of 3000 ms, a number of acquisition points setting of 18,000, and a sampling frequency of 200 kHz. The HSE sequence is used to scan the MRI sagittal image of different cores under saturated oil conditions, and the specific HSE sequence NMR experimental parameters are shown in Table 4.

(4) Core displacement: This step is the key to the success of the experiment. Firstly, the high-temperature and high-pressure circulation system is used to set the confining pressure to 2 MPa higher than the pressure at the inlet. Next, one pore volume (PV) of the prepared deuterium oxide is injected into the core from the inlet end of the core holder using an ISCO pump to simulate the injection process. Next, the valve at the outlet end of the core holder is closed, the injection pressure is increased until it stabilized at 10 MPa, and the valve at the inlet end of the core holder is closed. This process is maintained for 24 h to simulate the shut-in process. Finally, the valve at the inlet end and the outlet end are opened simultaneously to simulate the production process, and parameters such as injection volume, displaced fluid volume, and pressure are recorded by various sensors. The above procedure forms a complete displacement–imbibition coupling production process. Subsequently, NMR tests at different injection volume (1, 2, 3, and 4 PV) are conducted, and the experiment is terminated when the NMR spectra and MRI sagittal image do not change. For the continuous injection experiment, the confining pressure is also set at 2 MPa higher

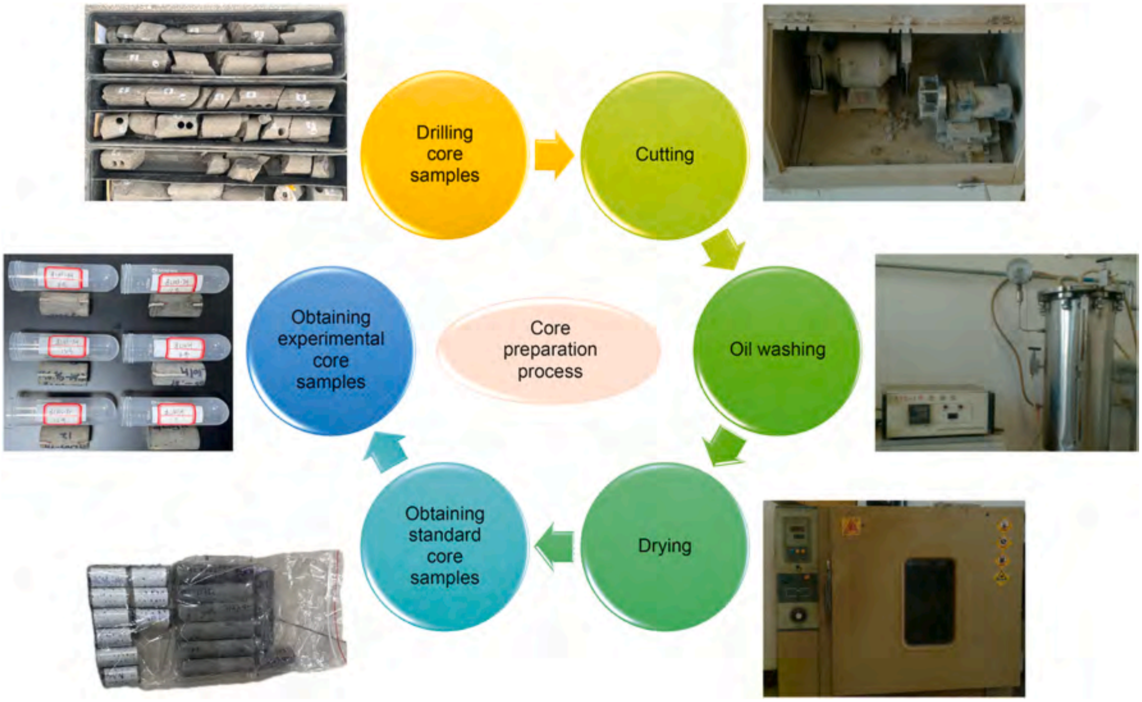

Fig. 4. Core preparation process for the oil–water two-phase displacement–imbibition experiments.

Table 3
Experimental design for oil–water two-phase displacement–imbibition experiments.

Influencing factor	Core sample No.	Lithology	Injection strategy
Different injection strategies	C9	Argillaceous tuff	Continuous injection
			Water huff and puff
			Displacement–imbibition
Different lithologies	C1	Argillaceous siltstone	Continuous injection
	C2		Water huff and puff
	C3		Displacement–imbibition
	C4	Vitric tuff	Continuous injection
	C5		Water huff and puff
	C6		Displacement–imbibition
	C7	Argillaceous tuff	Continuous injection
	C8		Water huff and puff
	C9		Displacement–imbibition
Different fracture penetration ratios	C9	Argillaceous tuff	Displacement–imbibition
	C10		
	C11		
Different fracture morphology	C9	Argillaceous tuff	Displacement–imbibition
	C12		
	C13		

Table 4
HSE sequence parameters for NMR experiments.

Parameter	Value
Flip angle, °	90
Refocus flip angle, °	180
RG, dB	20
PRG	3
DRG, dB	5
Phase encoding duration, ms	1
Sweep width, kHz	40
Dummy scan	0
TR, ms	500
TE, ms	2.44
Average	6
Read size	256
Phase size	192
Echo position, %	10

than the inlet pressure. Then, the prepared deuterium oxide with different volume is injected into the core from the inlet end of the core holder using an ISCO pump, and the valve at the outlet end is opened to simulate the process of continuous injection at the left end of the core and continuous production at the right end of the core. The NMR spectra and MRI sagittal image are scanned at different injection volume (1, 2, 3, and 4 PV) using the real-time NMR equipment. Finally, for the water huff and puff experiment, most steps are consistent with the displacement–imbibition experiment. However, during the production process after the shut-in stage, only the inlet valve is opened, while the outlet valve remains closed. The NMR spectra and MRI sagittal image are also captured at different injection volume (1, 2, 3, and 4 PV). In addition, for experiments focused on the influence of fracture complexity on the displacement–imbibition coupling effects, only the core sample is replaced, and the displacement–imbibition steps are repeated. This approach enables the analysis of how fluid flow characteristics and oil production from microscopic pores are affected by varying fracture penetration ratios and morphologies.

It is worth noting that the core sample size used in this study was constrained by the physical dimensions of the NMR/MRI equipment. The experimental setup requires samples to conform to a specific diameter and length for stable scanning and signal acquisition. As a result, longer core samples, which could potentially capture more continuous flow behavior and better represent field-scale heterogeneity, are not feasible within the current experimental framework. This limitation may restrict the generalizability of certain flow patterns observed, particularly those associated with larger-scale fracture–matrix interactions. Future research should consider adapting the experimental system to accommodate longer cores, enabling extended visualization and quantification of displacement–imbibition dynamics under more representative reservoir conditions.

2.3. Validation of the NMR experiment

To ensure the accuracy of our displacement–imbibition online NMR system, the volume of the experimental oil saturating each core sample was determined based on the difference between dry and wet weights pre- and post-vacuum saturation. The cores were then scanned using NMR to obtain the total signal, establishing a quantitative relationship between the experimental oil volume and the total NMR signal. The fitted curve, shown in Fig. 5, demonstrates a strong linear correlation between the oil volume and NMR signal ($R^2 = 0.9978$), underscoring the stability and precision of the NMR apparatus across repeated trials. This linear relationship supports the reliability of NMR signal variations in depicting oil saturation changes within the core samples. The relationship is described in Eq. (1).

$$V = 0.0001S - 0.3047 \tag{1}$$

2.4. NMR T_2 spectrum inversion and a new method of MRI image processing

2.4.1. Principle of NMR measurement

NMR technology is based on the principle of the magnetic response of hydrogen nuclei under an external magnetic field. This technique identifies key factors influencing fluid production and investigates the coupling effects within pore structures of porous

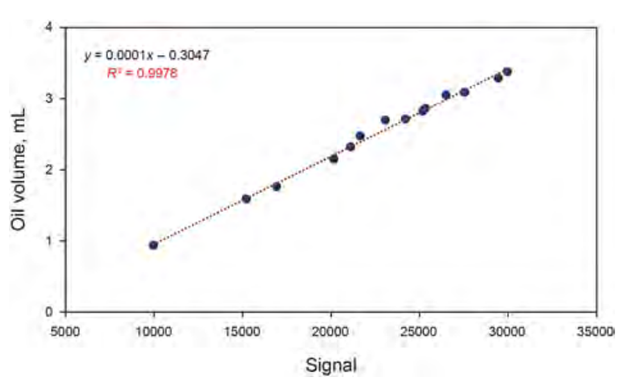

Fig. 5. Relationship between the total NMR signals and oil mass volume.

media, assisting in defining the range of movable fluids. This provides valuable insights for evaluating fluid utilization and understanding fluid migration patterns (Yuan et al., 2023). Currently, low-field NMR systems commonly utilize T_2 relaxation spectra and MRI to characterize fluid distribution. T_2 spectra indicate fluid utilization across different pore sizes, while MRI visualizes fluid distribution within specific axial slices of the core sample. MRI's non-invasive nature enables researchers to observe the internal structure of samples without damage, which is crucial for analyzing fluid distribution. In a low magnetic field, hydrogen nuclei in the sample are excited, generating radiofrequency signals closely related to the rock's pore structure. By detecting these signals and applying mathematical inversion, T_2 relaxation time spectra can be constructed to further characterize the rock's pore structure properties. The rock pore structure is studied by measuring these signals and establishing the T_2 relaxation time spectrum through mathematical inversion. The expression of relaxation time is

$$\frac{1}{T_2} = \frac{1}{T_{2\mathrm{B}}} + \frac{1}{T_{2\mathrm{S}}} + \frac{1}{T_{2\mathrm{D}}} \tag{2}$$

where T_2 is the total relaxation time, ms; $T_{2\mathrm{B}}$ is the transverse relaxation time of the filling fluid, ms; $T_{2\mathrm{S}}$ is the transverse relaxation time of the rock particle surface, ms; $T_{2\mathrm{D}}$ is the transverse relaxation time caused by fluid diffusion in the magnetic field gradient, ms.

Since the $T_{2\mathrm{B}}$ of the fluid is much larger than the T_2 of the saturated fluid in the core, and the $1/T_{2\mathrm{D}}$ caused by fluid diffusion is very small, these two terms can be ignored in the application process, that is, the relaxation time can be expressed as

$$T_2 = \frac{1}{\rho_{\mathrm{r}}\delta} r = Cr \tag{3a}$$

$$\delta = \frac{S}{V} r \tag{3b}$$

where ρ is the relaxation strength constant of the rock surface; δ is the pore shape factor; S is the surface area of rock particles, cm^2; V is the pore volume, cm^3; r is the average pore radius, cm; C is the conversion coefficient, μm/ms.

2.4.2. Division of pore-throat radius

Extensive research has demonstrated a strong correlation between pore-throat distribution measured by NMR tests and that obtained from high-pressure mercury intrusion (HPMI) tests (Wang et al., 2021; Zhang P.-F. et al., 2023). In this study, core samples from the Junggar east, Santanghu, and Niujuanhu areas are compared with their respective HPMI results (Fig. 6). The conversion coefficients (C) between NMR signals and pore-throat radius for the three areas are determined as 9.78, 8.45, and 70.29 nm/ms, respectively. Based on these values, relaxation times are subsequently converted to reflect pore-throat distribution. Since NMR can only detect hydrogen nuclei, the deuterium oxide signal is masked in the experiment, resulting in pore distribution reflecting solely the oil phase. During the displacement process, both oil saturation in the core samples and the amplitude of the NMR signal gradually decrease in tandem.

The core samples used in this paper are classified by NMR T_2 spectra as predominantly right-peaked bimodal. Considering the distinct migration mechanisms and dynamics across pores of different sizes, segmentation values are carefully selected based on the specific pore-throat structural characteristics of the target area. This segmentation allowed us to convert the NMR T_2

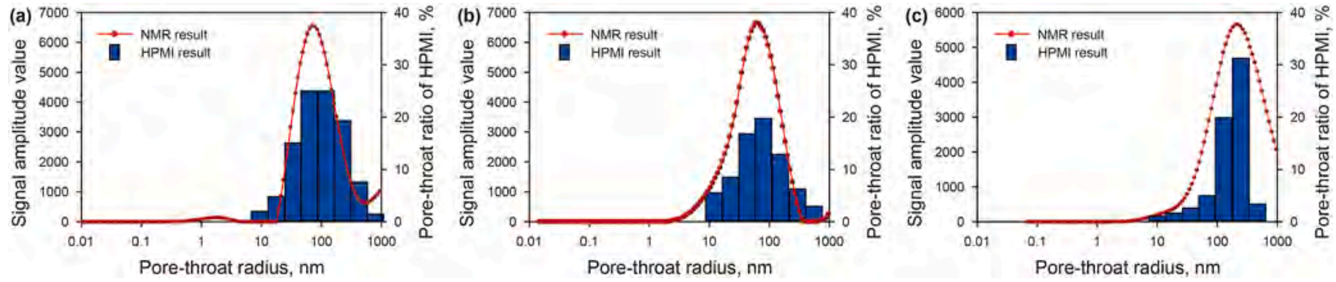

Fig. 6. The pore-throat distribution results obtained from HPMI tests and the NMR conversion results. (**a**) Junggar east area; (**b**) Santanghu area; (**c**) Niujuanhu area.

spectrum into detailed pore distribution maps (Fig. 7(a)). During the experimental process, NMR testing is conducted on cores from the Junggar, Santanghu, and Niujuanhu areas in both oil-saturated and post-displacement states, yielding pre- and post-displacement NMR spectra (Fig. 7(b)). Among them, the brownish-yellow area indicates residual oil saturation after displacement, and the produced oil is the difference between before and after displacement (the sum of the blue, green and red areas).

Therefore, based on the pore-throat interval division results, the utilization degree of pore-throat with different radii is determined by calculating the difference between the signal distribution area of a specific pore-throat interval and the initial saturation signal area, divided by the area between the initial saturation signal of the specific interval and the coordinate axis, as shown in Eq. (4). Subsequently, the contribution to oil displacement efficiency is quantified by calculating the ratio of the T_2 spectrum amplitude difference within a specific interval before and after displacement to the area difference between the entire T_2 spectrum and the x-axis before and after displacement, as shown in Eq. (5).

$$P(I) = \frac{\int_{T_{2a}}^{T_{2b}} [S_{\text{ini}}(T_2) - S_x(T_2)] \mathrm{d}T_2}{\int_{T_{2a}}^{T_{2b}} S_{\text{ini}}(T_2) \mathrm{d}T_2} \tag{4}$$

$$E(I) = \frac{\int_{T_{2a}}^{T_{2b}} [S_{\text{ini}}(T_2) - S_x(T_2)] \mathrm{d}T_2}{\int_{T_{2,\min}}^{T_{2,\max}} [S_{\text{ini}}(T_2) - S_x(T_2)] \mathrm{d}T_2} \tag{5}$$

where $S_{\text{ini}}(T_2)$ and $S_x(T_2)$ denote the NMR T_2 amplitude distribution before and after displacement, respectively; $P(I)$ quantifies the utilization degree of pores within the interval $I = [T_{2a}, T_{2b}]$ by normalizing the spectral amplitude reduction to the initial signal area of the same interval; $E(I)$ evaluates the relative contribution of pores in interval I to the overall displacement efficiency by comparing the local amplitude reduction to the total spectral reduction over the entire T_2 range $[T_{2\min}, T_{2\max}]$.

2.4.3. New method of MRI image processing

MRI is a powerful tool for studying the displacement–imbibition coupling process, as it can reflect changes in oil–water distribution within the core based on signal intensity (brightness of color). However, conventional MRI images only provide relative variation trends and are limited in their ability to quantitatively characterize oil saturation changes across different core regions. Similarly, although the overall saturation change can be estimated by calculating the total oil production before and after displacement, this approach lacks spatial resolution and cannot capture local saturation information. To address these limitations, this study proposes a novel method that integrates image processing with inversion modeling to quantitatively characterize oil saturation in different core regions before and after displacement. This approach overcomes the traditional limitations of MRI by enabling quantitative evaluation of local saturation changes within the core. The specific methodology is as follows:

First, the MRI data volume is preprocessed using a programmed approach. The signal intensity is normalized to the RGB color scale range (0–255) through min–max normalization, which enables consistent visualization and facilitates quantitative analysis. The normalization formula is as follows:

$$x = 255 \times \frac{S_{\text{i}} - S_{\min}}{S_{\max} - S_{\min}} \tag{6}$$

where x represents the normalized pixel value; S_{i} is the original MRI signal intensity; and $S_{\min}$ and $S_{\max}$ are the minimum and

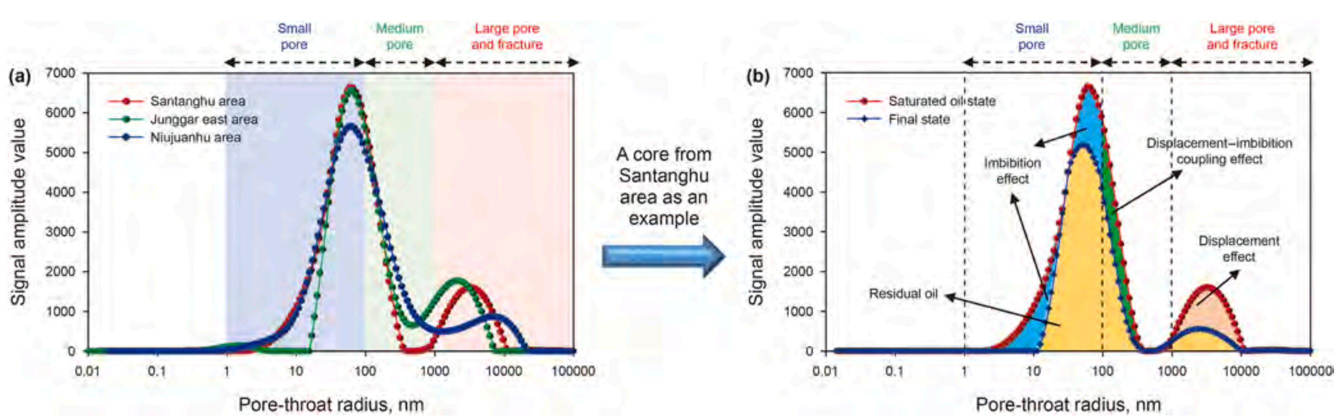

Fig. 7. (**a**) Interval division of pore-throat radius under saturated oil state. (**b**) A schematic diagram illustrating the evaluation principles of different effects in the displacement–imbibition coupling process.

maximum signal intensities across all MRI data volumes of the experimental cores. The normalized value x is directly correlated with color brightness: the redder the color (i.e., the higher the value of x), the stronger the signal intensity, indicating greater oil saturation. This suggests that the corresponding region may contain significant residual oil.

We found that regions with high x values, often located near fractures or flow-dead zones, exhibit poor mobility and retention characteristics. The changes in oil saturation within these regions follow a clearly nonlinear trend. Therefore, traditional linear models are insufficient to characterize the spatial distribution of saturation accurately. To address this, and based on experimental observations and reservoir flow mechanisms, this study introduces a logarithmic model combined with a linear term to construct a saturation fitting function. This approach provides a more accurate and physically meaningful description of the relationship between the normalized signal intensity x and oil saturation:

$$f(x, a, b, c) = a\ln(x + b) + cx \tag{7}$$

This model introduces a linear term to the logarithmic function to accommodate the varying response characteristics across different regions. The physical meanings of the fitting parameters are as follows:

- Parameter a: Controls the curvature of the saturation response in low signal intensity regions, reflecting the sensitivity of saturation changes in low-saturation zones.
- Parameter b: Shifts the entire function horizontally to ensure the validity of the logarithmic term's domain and adjusts the initial response range of saturation.
- Parameter c: Represents the linear growth trend of saturation in high signal regions, enhancing the model's ability to capture the overall trend.

To verify the adaptability and physical relevance of the proposed model, we systematically adjusted the values of parameters a, b, and c, and plotted the response curves under different parameter combinations (Fig. 8). These curves illustrate the influence of each parameter on the predicted oil saturation. Experimental results demonstrate that the model exhibits strong flexibility and can be effectively calibrated to match the characteristics of actual reservoirs, thereby improving the accuracy of oil saturation prediction across heterogeneous core samples.

Subsequently, by integrating the overall oil production data from the displacement–imbibition coupling production experiment, the model was subjected to parameter inversion and nonlinear fitting (Fig. 9(a)), resulting in the following optimal expression:

$$y = 18.034\ln(x + 1) - 6.78 \times 10^{-6}x \tag{8}$$

The fitted curve shows excellent agreement with the experimental data, achieving a coefficient of determination of $R^2 = 0.9952$, indicating high accuracy and stability of the model (Fig. 9(b)). In this expression, the logarithmic term primarily determines the overall trend of the model, while the linear term fine-tunes the response in the high-value range, enhancing the model's ability to capture subtle variations in oil saturation.

By substituting the x value of each pixel into the fitted function, the corresponding oil saturation for each pixel is calculated. Subsequently, by averaging or integrating the saturation values across all pixels in the image, the overall change in average oil saturation of the core before and after displacement can be determined

$$\Delta S_{\text{total}} = \frac{1}{N}\sum_{i=1}^{N}\left(S_i^{\text{before}} - S_i^{\text{after}}\right) \tag{9}$$

where ΔS_{total} is the change in average oil saturation; N is the total number of valid pixels in the image; and S_i^{before} and S_i^{after} are the oil saturation at the same pixel location before and after the displacement process, respectively.

Meanwhile, to further investigate the differential responses of various regions—such as fracture-dominated regions, matrix

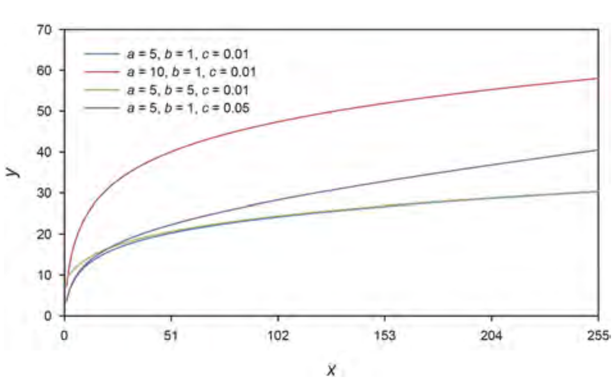

Fig. 8. Response curves of the target model with different parameter combinations.

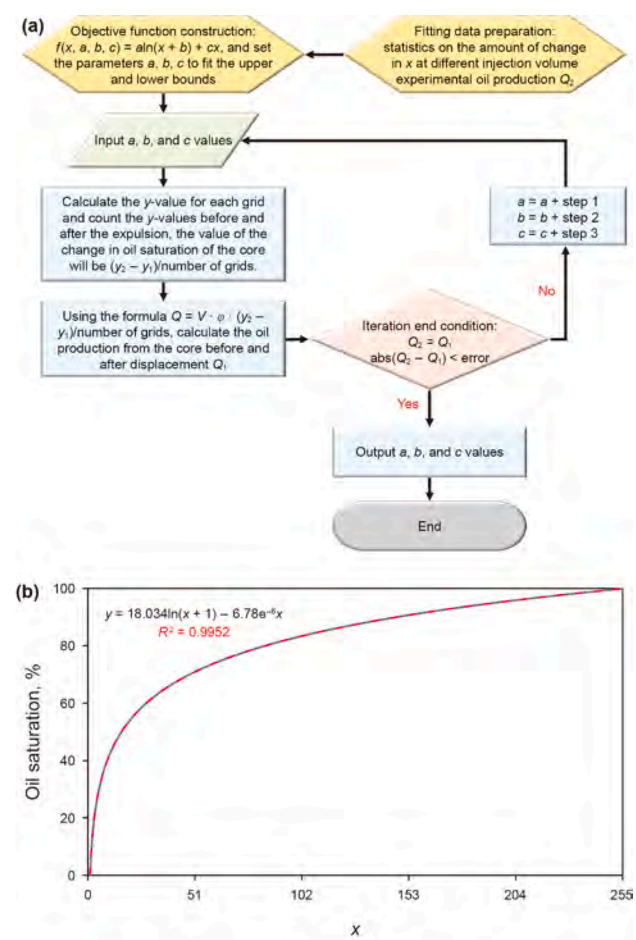

Fig. 9. (**a**) The flowchart for the inversion fitting process of the relationship curve. (**b**) The relationship between oil saturation and variable x.

regions, and heterogeneous interfaces—during the displacement–imbibition coupling production, this study applies an automated segmentation algorithm to divide the core images into multiple regions of interest (ROI). The oil saturation change within each ROI is then calculated individually:

$$\Delta S_{\mathrm{ROI}} = \frac{1}{M}\sum_{j=1}^{M}\left(S_j^{\mathrm{before}} - S_j^{\mathrm{after}}\right) \tag{10}$$

where ΔS_{ROI} is the average oil saturation change in that region; M is the number of pixels within a given ROI; and S_j^{before} and S_j^{after} are the saturation values at pixel j within that region, before and after displacement. By comparing the oil saturation change ΔS across different regions, a quantitative analysis of oil–water migration between the matrix and fractures can be performed. This enables the identification of potential channeling pathways or fluid retention zones, thereby helping to uncover the spatial heterogeneity of the displacement–imbibition coupling effect.

Using this method, the study achieves quantitative estimation of oil saturation in different regions based on MRI images without compromising the integrity of the core structure. Specifically, saturation changes across the entire core can be obtained by performing pixel-wise difference calculations between pre- and post-displacement images. In addition, any ROI can be selected for statistical analysis, enabling the extraction of local oil saturation evolution. This approach provides an efficient and accurate technique for investigating the fluid displacement–imbibition coupling mechanisms in complex and heterogeneous reservoirs. It offers important theoretical insights and engineering guidance for understanding and optimizing coupling effects between matrix and fracture, thereby enhancing the design and evaluation of EOR strategies in tight and shale reservoirs.

3. Results and discussion

3.1. Oil–water transport mechanisms of cores with different injection strategies

MRI imaging along the fracture orientation of the core samples is conducted to obtain images corresponding to different injection volume. Fig. 10 illustrates the evolution of oil saturation in the cores from the Junggar east area under three different injection strategies: continuous injection, water huff and puff, and displacement–imbibition coupling production. Fig. 11 illustrates the evolution of NMR T_2 spectra for the Junggar east cores under various injection strategies, alongside a visual comparison of the actual cores before and after displacement. For core sample C1, due to poor connectivity of the pore-throat network, the oil phase within the matrix is difficult to utilize, with the injected water primarily displacing oil from the large pores and fractures. As the injection volume increases, the reduction in oil signals within the fractures becomes progressively less pronounced, exhibiting a diminishing trend, while the oil signals in both small and medium pores remain nearly unchanged. By fitting the peaks of the T_2 spectra, the migration trend of crude oil within the pores can be obtained (black line in Fig. 11). As continuous injection progresses, the trend lines for small pores and large pores exhibit a leftward inclination, indicating a slight shift of the spectral peaks toward the left. Analysis indicates that upon water injection into the core, the injected water initially invades the large pores due to their lower flow resistance. This results in the displacement of crude oil from the large pores, leading to a decrease in signal intensity. Concurrently, under the displacement effect, the injected water extracts a small portion of crude oil from the small pores, but most of the oil phases of the small pores are minimally transported to the smaller scale pores. This migration behavior causes a leftward shift of the NMR T_2 spectral peaks. For core sample C2, oil utilization primarily occurs within the large pores in contact with the imbibition end on the left side, driven by capillary imbibition. In contrast, crude oil within the small pores of the internal matrix and the fractures on the right end remains largely unrecovered, leaving a substantial amount of residual oil. Analysis of the migration trends in the T_2 spectral peaks reveals that the trend lines for small pores and large pores also exhibit a leftward inclination, with a more pronounced decrease in signal intensity within fractures. This observation indicates that water huff and puff enhance the capillary imbibition, utilizing the large pores surrounding the fractures, as illustrated in the core image in Fig. 11 (b). For core sample C3, under displacement–imbibition coupling effects, the amount of crude oil in the core matrix is significantly reduced compared to that in cores subjected to continuous injection and water huff and puff. The oil phases in small pores, medium pores, and large pores are progressively extracted, leading to a continuous decline in signal values. Meanwhile, the T_2 spectral peak trend also exhibits a leftward inclination. However, the inclination of the large pores trend line is noticeably steeper than that of the small pores. This difference arises because, under the

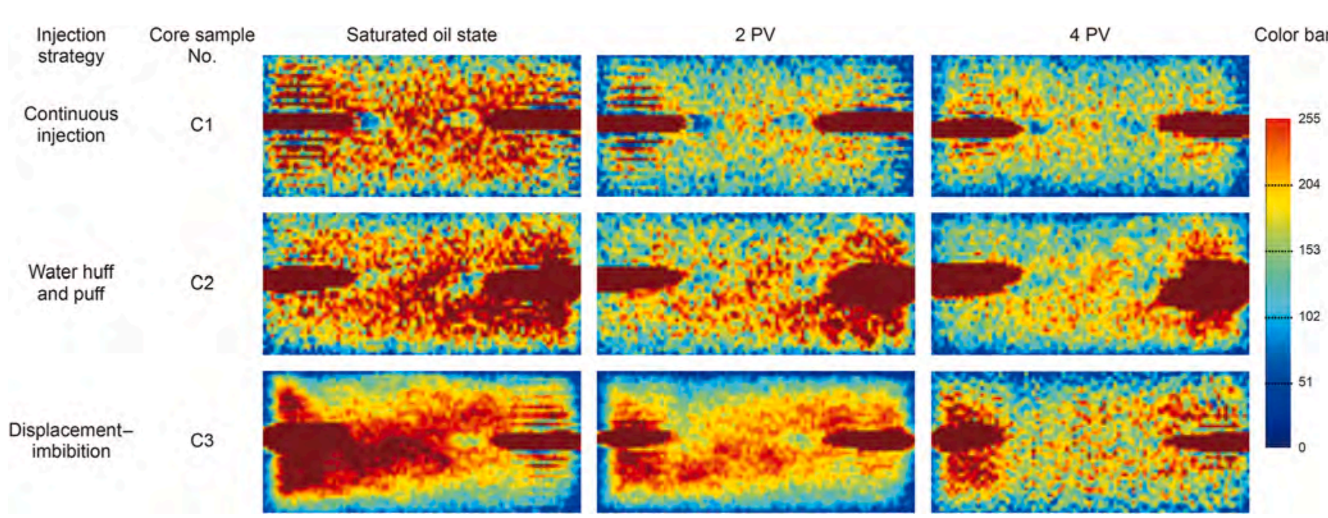

Fig. 10. Oil saturation distribution at various stages of different injection strategies for cores from the Junggar east area.

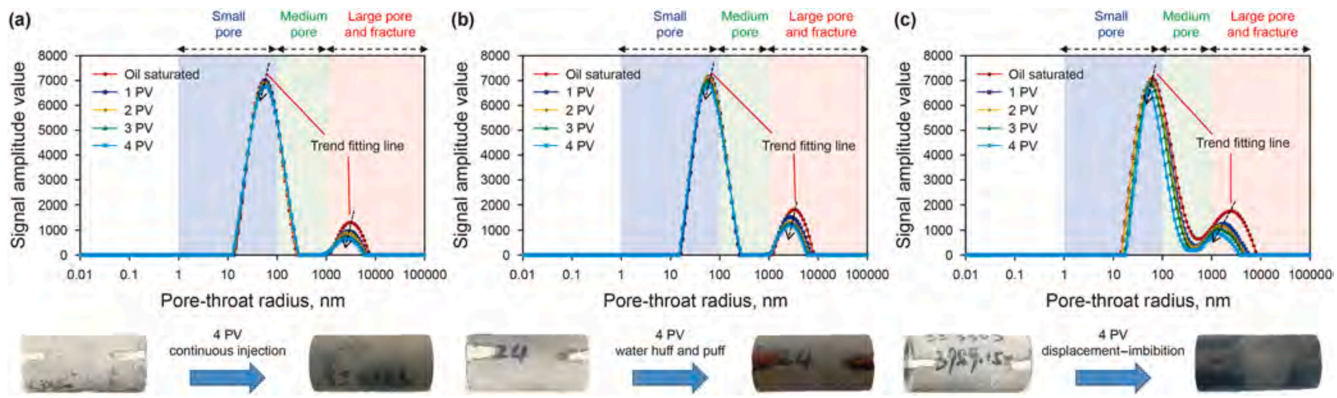

Fig. 11. NMR T_2 spectral evolution and core comparison images under different injection strategies for cores from the Junggar east area. (**a**) Continuous injection process; (**b**) water huff and puff process; (**c**) displacement–imbibition process.

displacement–imbibition coupling effects, the exchange of fluids and oil among small pores, medium pores and large pores becomes more frequent. Consequently, oil migrates more readily from the matrix pores to the fractures, where it is extracted. Nevertheless, due to the relatively tight nature of the core, utilizing the oil saturation remains challenging, and a portion of the residual oil persists within the core matrix.

Unlike the dense cores from the Junggar east area, the cores from the Niujuanhu area exhibit well-developed natural fractures (as shown in the core images in Fig. 13). These natural fractures, combined with the artificial fractures, form a complex fracture network that facilitates the extraction of crude oil from the cores. As shown in Fig. 12, the continuous injection process primarily utilizes the matrix large pores along the mainstream line for core samples with well-developed fractures and high connectivity (core samples C4, C5, and C6). When large pores and fractures form the water-driven advantage channel, a significant amount of water flows along the channel, bypassing residual oil regions resulting in ineffective water injection. Consequently, residual oil remains trapped within the core, further complicating effective displacement. During the water huff and puff process, imbibition is significantly enhanced in fractured cores due to the increased contact area between pores and fractures. This facilitates the stepwise migration of crude oil from smaller pores to larger pores and fractures. Accordingly, the change in the oil saturation field within the core is more pronounced compared to that observed during continuous injection. Under the displacement–imbibition coupling effects, the swept volume of injected water and the recoverable oil significantly increase. The frequent fluid exchange between the core matrix and fractures induces pressure oscillations within the matrix pore-throat system. This effect facilitates the displacement of crude oil from smaller pores, gradually “shaking” it out under the coupled mechanism. Therefore, the overall oil saturation of the core decreases significantly. It is worth noting that the presence of fractures effectively enhances the permeability of the core. However, it can also lead to water channeling, which may reduce the overall utilization degree. Therefore, preventing water channeling is crucial. A detailed analysis of the influence of fractures on the displacement–imbibition coupling process will be provided in the subsequent discussion. Simultaneously, NMR T_2 spectra are tested for the Niujuanhu cores under different injection strategies (Fig. 13), and the migration trend lines of the T_2 spectrum peaks are fitted accordingly. In contrast to the cores from the Junggar east area, the small pore trend line in the cores from the Niujuanhu area exhibits an inclination angle of 90° during the continuous injection process, indicating a linear decline in oil content within small pores. However, during water huff and puff and displacement–imbibition processes, the small pore trend lines incline rightward, with a more pronounced inclination observed in

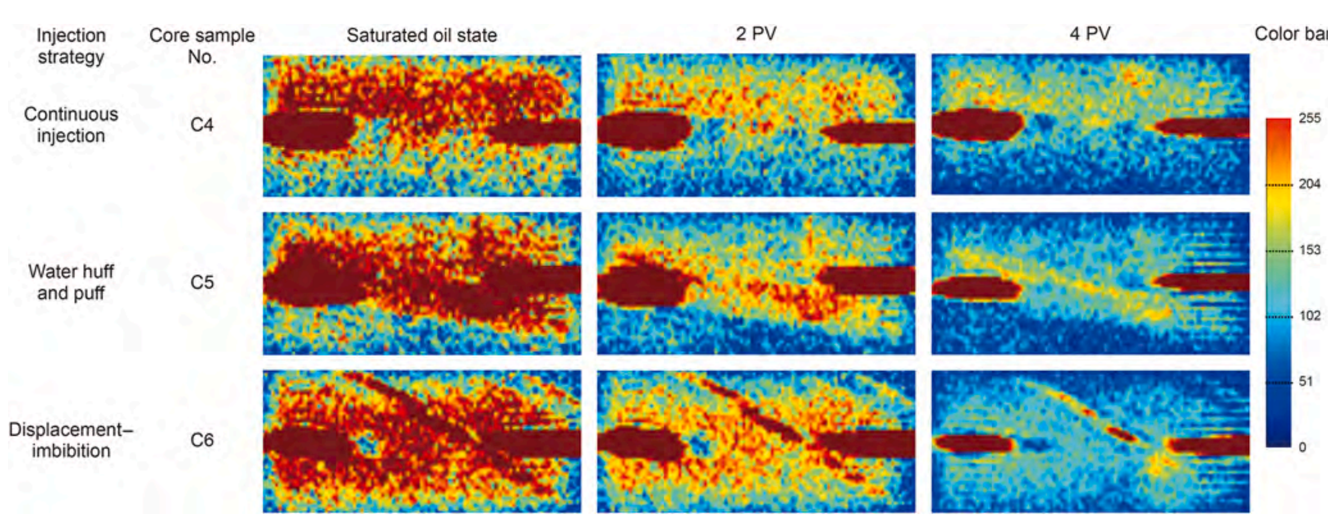

Fig. 12. Oil saturation distribution at various stages of different injection strategies for cores from the Niujuanhu area.

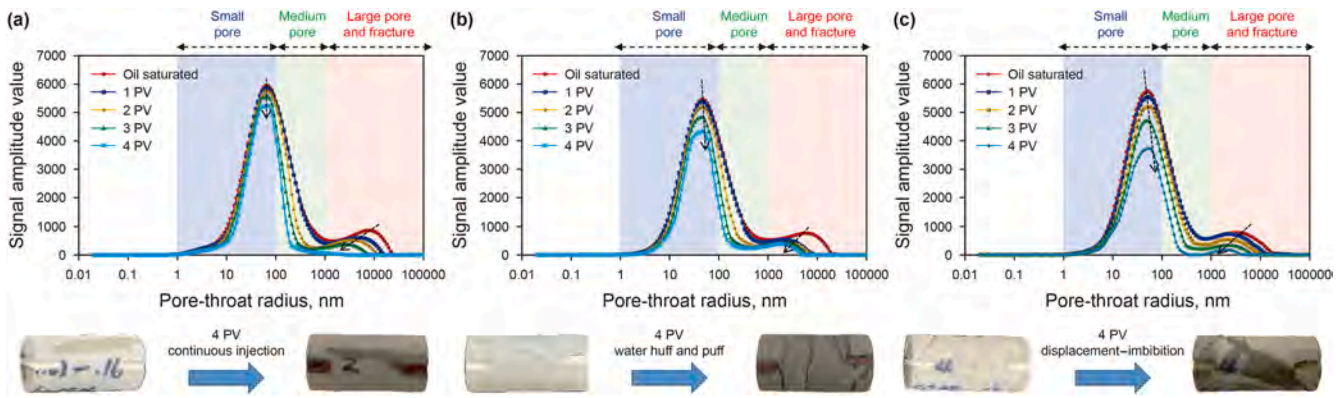

Fig. 13. NMR T_2 spectral evolution and core comparison images under different injection strategies for cores from the Niujuanhu area. (**a**) Continuous injection process; (**b**) water huff and puff process; (**c**) displacement–imbibition process.

the displacement–imbibition process. This behavior highlights the critical role of fractures in facilitating the recovery of oil from small pores. As the injection volume increases, the decline in T_2 spectrum values becomes more conspicuous, indicating that once the displacement–imbibition coupling effects extend throughout the pore structure of the core, the exchange between the injected water and oil becomes more efficient, resulting in higher oil recovery. In addition, the trend line for large pores is similar to that observed in the Junggar east cores, exhibiting a leftward inclination. Among the injection strategies, the angle of inclination is the steepest for continuous injection, followed by displacement–imbibition, and the smallest for water huff and puff. This phenomenon occurs because the oil in large pores is primarily extracted through displacement mechanisms. Since the displacement effect is most significant during continuous injection, the T_2 spectrum shows the greatest decline, resulting in the steepest trend line inclination.

The pore-throat structure of the cores from the Santanghu area exhibits greater heterogeneity, with a more dispersed pore size distribution that lies between those of the Junggar east and Niujuanhu areas (Fig. 7(a)). Therefore, although the cores from the Santanghu area lack the extensively developed natural fractures observed in the Niujuanhu area, their pore-throat distribution characteristics and the presence of partial fractures enable better displacement performance under different injection strategies compared to the Junggar east cores. However, the displacement effectiveness is slightly inferior to that of the Niujuanhu cores (Fig. 14). Similarly, the trend lines of the NMR T_2 spectral peaks for the Santanghu cores closely resemble those observed in the Niujuanhu area. The oil migration trend lines for smaller pores exhibit a rightward inclination, suggesting that, under the displacement–imbibition coupling effects, the matrix oil gradually migrates in small quantities toward larger pores (Fig. 15). This migration establishes an ‘oil supply chain’ that progresses from small pores to larger pores and ultimately to fractures. Furthermore, the trend line of crude oil migration in the large pores is inclined to the left, which indicates that the crude oil in the large pores of the core can be effectively driven out under different injection strategies.

3.2. Microscopic oil–water displacement mechanism in different pores

The microscopic displacement mechanisms in pores and fractures of varying sizes form the theoretical foundation for the efficient development of shale oil reservoirs. To better illustrate the microscopic displacement mechanisms under different injection strategies, we select core samples from the Santanghu area, which exhibit moderate development performance, as the research focus. Fig. 16(a) illustrates the evolution of NMR T_2 spectra for three core samples before and after displacement under different water injection strategies. A clear decline in spectral peak values is observed, indicating that the injected water effectively utilized oil in pores of various sizes, resulting in efficient oil production from the cores. By comparing continuous injection, water huff and puff, and displacement–imbibition processes, it is evident that displacement–imbibition is more effective in utilizing oil from small, medium, and large pores. Both continuous injection and water huff and puff processes exhibit certain limitations and fail to achieve comprehensive utilization of the core. Fig. 16(b) illustrates the relationship between pore-throat utilization degree and the injection volume under different water injection strategies for the Santanghu cores. Notably, pores of different scales exhibit a trend of initially rapid growth followed by slower growth. During the continuous injection process, the injected water primarily promotes oil production in medium and large pores. After 4 PV of displacement, the utilization degree of medium and large pores increases from 6.31% and 45.94% to 26.04% and 83.14%, respectively, whereas the utilization degree of small pores reaches only 10.87%. This is attributed to the strong resistance caused by the smaller capillary radius and the Jamin effect at the pore-throat. Therefore, the continuous injection process primarily relies on displacement mechanisms to utilize oil from medium and large pores.

For the water huff and puff process, it is observed that the utilization degree of medium pores exhibits negative values in the early stages. This phenomenon is mainly attributed to three factors: (1) During the water injection stage, water can transport oil into medium pores, leading to a redistribution of oil within the core. (2) Under the influence of capillary forces, oil migrates inversely from small pores to medium pores via imbibition. (3) Oil in large pores may flow back into medium pores through positive imbibition. These phenomena collectively result in an increase in oil content in medium pores. As the injection volume increases, capillary imbibition gradually strengthens, leading to the continuous displacement of oil from small pores, with the oil displacement efficiency reaching 24.31%. However, compared to continuous injection, the displacement effect during the water huff and puff process is significantly weaker, with the utilization of medium and large pores at 10.97% and 52.88%, respectively. Thus, the water huff and puff process primarily relies on capillary imbibition to displace oil within small pores.

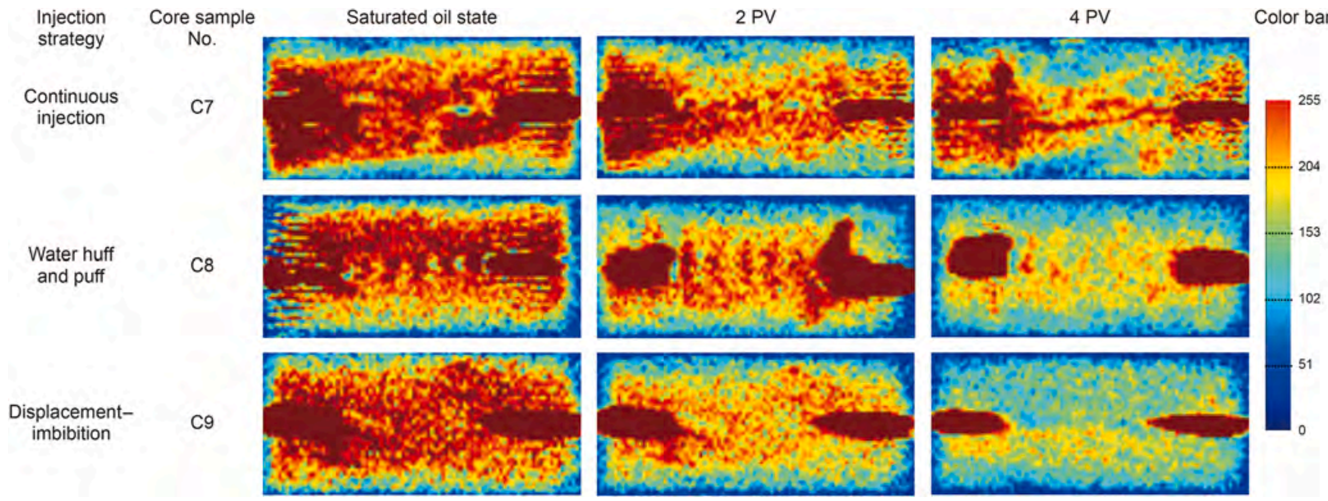

Fig. 14. Oil saturation distribution at various stages of different injection strategies for cores from the Santanghu area.

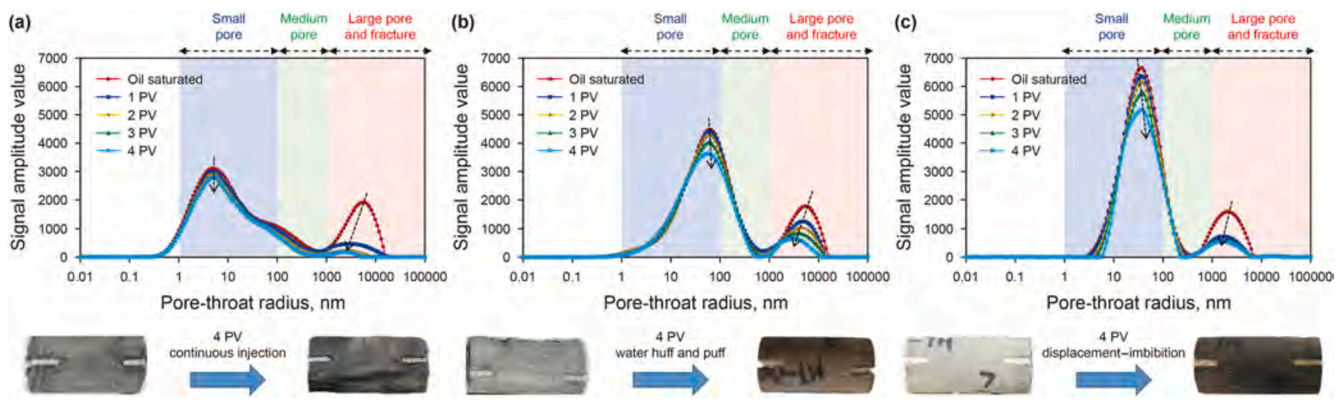

Fig. 15. NMR T_2 spectral evolution and core comparison images under different injection strategies for cores from the Santanghu area. (**a**) Continuous injection process; (**b**) water huff and puff process; (**c**) displacement–imbibition process.

Unlike water injection strategies that depend solely on a single driving force (either displacement or imbibition effect), the displacement–imbibition coupling production mechanism leverages multiple driving forces (displacement–imbibition effect) to utilize pores of different scales. The ultimate utilization rates of small, medium, and large pores increase from 16.80%, 5.04%, and 26.47% to 32.21%, 24.13%, and 66.11%, respectively. Moreover, pore-throat utilization during the displacement–imbibition coupling process is predominantly concentrated in the early stages and gradually diminishes later. This indicates that displacement–imbibition coupling effectively lowers the utilization threshold of pores, resulting in higher oil displacement efficiency. Additionally, the oil recovery performance under different injection strategies is summarized (Fig. 16(c)). As shown in the figure, the overall final oil displacement efficiency of displacement–imbibition coupling production (22.04%) is higher than that of continuous injection (16.29%) and water huff and puff (13.99%). However, in the early stages of displacement, the oil displacement efficiency of water huff and puff exceeds that of continuous injection. This is due to the fact that the mainstream channel has not yet been formed within the core during the early stages of continuous injection. In contrast, the early stages of water huff and puff involve significant imbibition replacement at the matrix–fracture interfaces, resulting in higher oil production and thus higher oil displacement efficiency. The contributions of different pore sizes to oil displacement efficiency are also analyzed (pie charts in Fig. 16(c)). For both continuous injection and water huff and puff, more than 70% of the oil displacement efficiency is attributed to the extraction of oil from large pores, while small and medium pores contribute only about 30%. This suggests that some of the residual oil in medium and small pores is connected through smaller pore-throat channels, indicating the untapped potential of small and medium pores in enhancing oil recovery (EOR). Under displacement–imbibition coupling effects, the contribution of small and medium pores to oil displacement efficiency increases by approximately 20%, reaching about 50%. This approach effectively recovers the residual oil that cannot be utilized by the other two injection strategies and achieves balanced utilization across pores of different scales. Clearly, displacement–imbibition coupling production is a superior method for EOR, as it maximizes the contribution of underutilized pore networks and ensures more comprehensive utilization of residual oil.

Generally, displacement–imbibition coupling production can be divided into three stages (Fig. 17). The first stage is the water injection stage, dominated by the displacement effect. At this stage, the injected water, driven by pressure, infiltrates the core matrix through fractures, as fractures possess higher permeability and lower flow resistance. Subsequently, most of the oil in large pores is displaced by the displacement effect. Simultaneously, due to the combined effects of viscous forces and capillary forces,

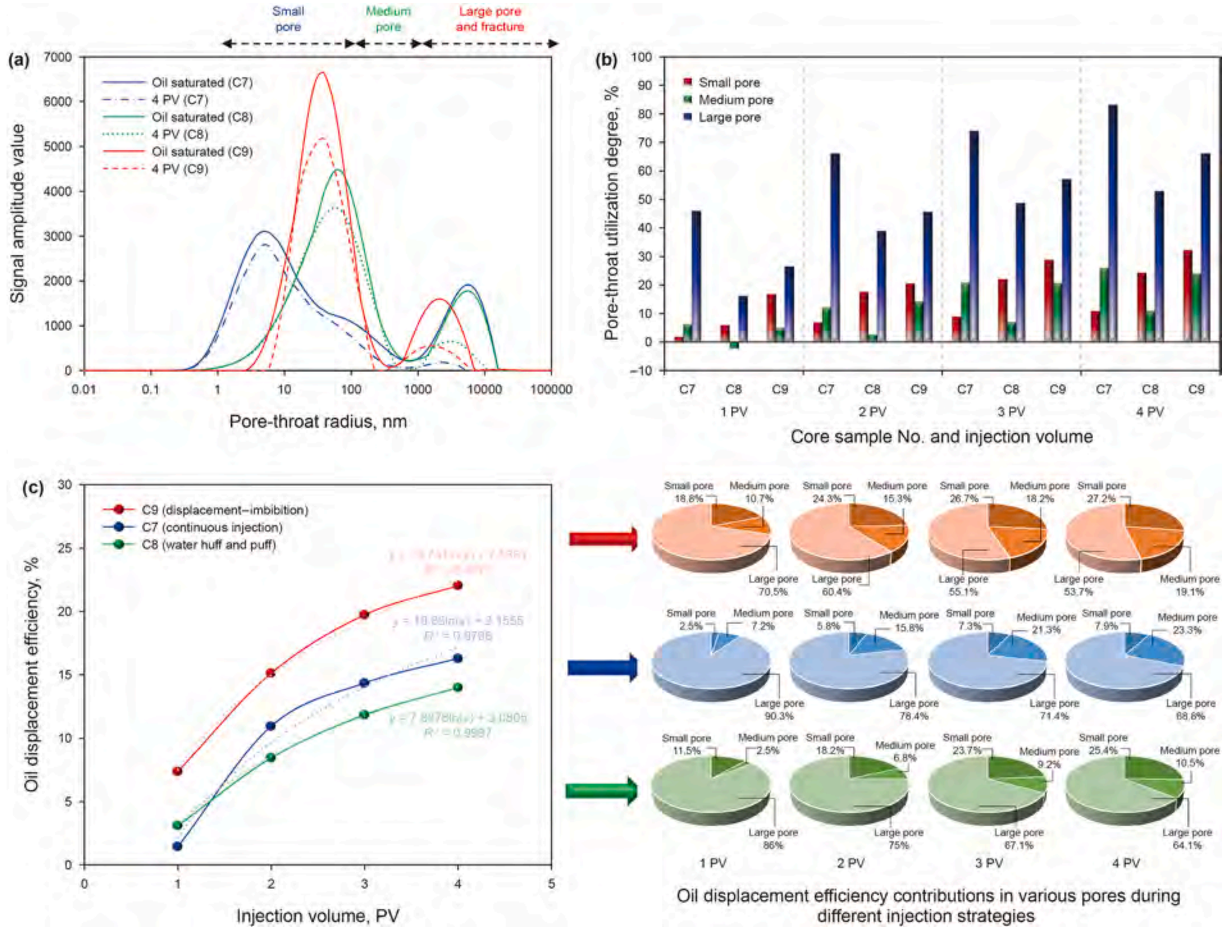

Fig. 16. (**a**) NMR T_2 spectral evolution of Santanghu cores before and after displacement under different injection strategies. (**b**) Relationship between pore-throat utilization degree and injection volume for Santanghu cores under different injection strategies. (**c**) Oil recovery performance of different injection strategies and the contributions of various pore sizes to oil displacement efficiency.

localized cocurrent imbibition occurs at the interface between the fractures and the matrix, enabling oil to be expelled from the pores. Under pressure differential driving, mainstream channels are established within the matrix pores, facilitating effective displacement in some large pores. This stage is primarily characterized by oil recovery driven by the displacement effect and the partial cocurrent imbibition effect. The second stage is the shut-in stage, dominated by capillary imbibition. During this stage, pressure gradually propagates into pores of varying sizes, expanding the range of influence. Near the interface between the matrix and fractures, as the pressure differential between pores decreases, pore-throat radius shrinks, and capillary pressure increases, the displacement effect diminishes significantly, leading to reduced utilization in fractures and large pores. However, water within fractures and large pores undergoes counter-current imbibition into the smaller pores of the matrix. The oil films on the walls of small pores are gradually replaced by water, forcing the oil out of small pores into larger ones or fractures, resulting in counter-current imbibition. In regions near the mainstream channels within the matrix, the pressure drop initiated during the water injection stage continues to propagate. When pressure exceeds capillary forces, cocurrent imbibition occurs in some pores at this stage. However, as the pressure drops below capillary forces, localized high-pressure zones form within the matrix pores. Counter-current imbibition then overcomes the displacement pressure differential, transferring oil from small pores to larger ones. Thus, during this stage, under the coupling effects of cocurrent and counter-current imbibition, oil within the matrix pores is extensively recovered, making this stage the primary contributor to overall oil production. The third stage is the production stage, dominated by displacement–imbibition coupling effects. After the shut-in stage, oil from the complex tortuous small pores migrates into larger pores or fractures. At this point, the re-established pressure differential displacement system utilizes the oil from the large pores and fractures. Simultaneously, the displacement effect and imbibition effect within the matrix achieve dynamic equilibrium, with their magnitudes diminishing compared to the water injection and shut-in stages. Eventually, the fluid distribution within the matrix pores reaches a stable state.

Compared to conventional water injection methods, displacement–imbibition coupling production enhances oil recovery by artificially altering the pressure field within the matrix pores, creating localized high-pressure differentials. This induces pressure oscillations between pores of different sizes, effectively activating and leveraging capillary imbibition, lowering the utilization threshold for pore-throat networks. Over multiple cycles of displacement–imbibition coupling production, oil trapped in hard-to-utilize pores is gradually displaced through continuous "oscillations." This oil–water flow process across various pore sizes is inherently prolonged. The key to displacement–imbibition coupling production is pressure oscillation and capillary imbibition. Notably, imbibition does not only occur near the matrix–fracture interface, nor is it limited to the early stages of the process. Instead, imbibition persists throughout the entire

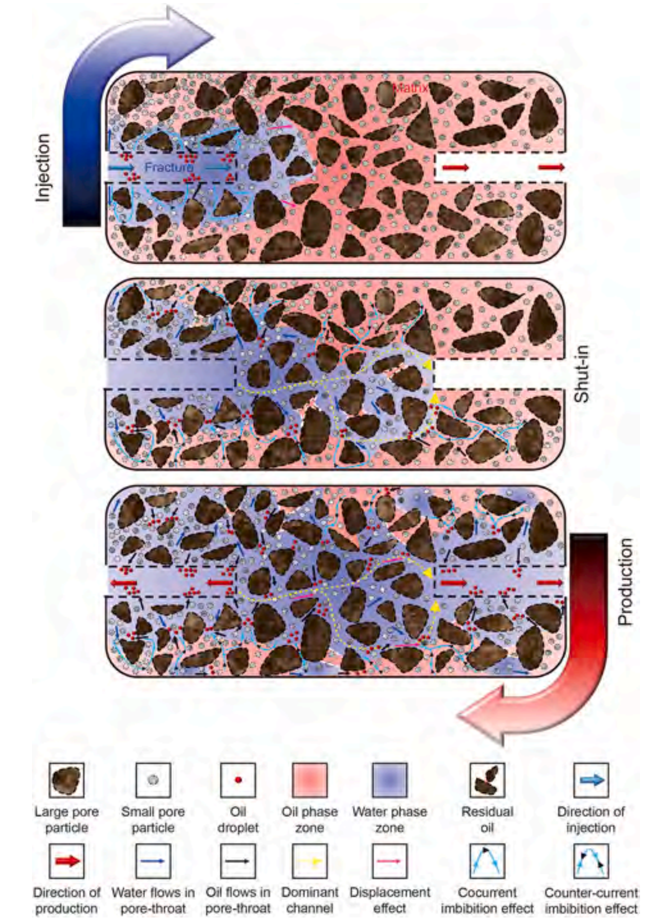

Fig. 17. Schematic diagram of fluid transportation at different stages of oil–water two-phase displacement–imbibition coupling oil production.

displacement–imbibition coupling production process within the matrix pores, playing a continuous and vital role.

3.3. Influencing factors for displacement–imbibition coupling production

After a comparative analysis of different injection strategies, the displacement–imbibition coupling production is identified as a superior approach for EOR. However, for tight and shale reservoirs, the performance of this method is influenced by multiple factors, among which the lithology of reservoir rocks and the heterogeneity of matrix–fracture systems are the most critical. Based on an online displacement–imbibition NMR system, this study systematically investigates the effects of lithology, fracture penetration ratio, and fracture morphology on the efficiency of displacement–imbibition coupling production. Experimental data, including MRI images and NMR T_2 spectra, are used to calculate the ultimate oil displacement efficiency and the contributions from pores of different scales. The pore-throat utilization degree during the production process is quantitatively evaluated, and the contribution of different actions to the oil displacement efficiency is also analyzed. These findings provide crucial insights for optimizing field production design in complex reservoirs.

3.3.1. Effect of lithology

Fig. 18 illustrates the changes in oil saturation for cores of different lithologies during displacement–imbibition coupling production. The initial oil saturated state reveals distinct characteristics for each lithology. The argillaceous siltstone from the Junggar east area exhibits a homogeneous pore distribution due to compaction effects. In contrast, the vitric tuff from the Niujuanhu area and the argillaceous tuff from the Santanghu area show strong pore heterogeneity. Additionally, a natural fracture is observed in the vitric tuff core, further emphasizing the lithological differences in oil saturation characteristics. For the argillaceous siltstone core sample C3, the poor pore-throat connectivity due to its tight nature limits the effectiveness of the displacement–imbibition coupling production method. The overall oil saturation of the core decreases only slightly, with partial utilization confined to the mainstream channel in the core's central region, leaving a substantial amount of residual oil within the matrix. This indicates that the applicability of displacement–imbibition coupling production is relatively low for the argillaceous siltstone matrix in the Junggar east area, necessitating consideration of other factors to enhance its development efficiency. For the vitric tuff core C6, the excellent pore-throat connectivity allows significant utilization of oil in both the pores and fractures under the displacement–imbibition coupling effects. The presence of natural fractures, combined with artificially induced fractures, forms a complex fracture network, increasing the contact area between the matrix and fractures. This enhances the interaction frequency and facilitates the exchange of fluids with the residual oil in the pores, leading to oil migration from matrix pores to fractures and ultimately reducing the overall oil saturation of the core. For the argillaceous tuff core sample C9, the change in oil saturation is primarily concentrated in the upper part of the core. This is due to the strong heterogeneity of the core from the Santanghu area, which results in uneven pore distribution. The coupling effects of imbibition (capillary force) and displacement (viscous force) help drive the oil out of the larger pores or fractures, thereby improving the core's oil displacement efficiency.

Fig. 19(a) presents the evolution of NMR T_2 spectra before and after the displacement–imbibition coupling production for cores of different lithologies. Compared to the core sample C3 with poor pore-throat connectivity, the core samples C6 and C9, which exhibit better pore-throat connectivity, show a more pronounced decrease in the oil signals in small, medium, and large pores after the experiment. The T_2 spectra gradually decrease and shift to the right, indicating that the oil within the matrix slowly migrates into fractures under the influence of the displacement–imbibition coupling effects. As a result, the matrix pores continue to supply oil to the fractures. Fig. 19(b) shows the relationship between pore-throat utilization and the injection volume during the displacement–imbibition coupling production for cores of different lithologies. It is observed that under the displacement–imbibition coupling effects, the largest pore-throat utilization occurs in large pores, followed by medium and small pores. Among them, the vitric tuff core, with its developed fractures and good pore-throat connectivity, exhibits the highest utilization degree in pores of different sizes. After 4 PV of displacement–imbibition coupling production, the utilization degree for small, medium, and large pores reaches 59.23%, 35.70%, and 79.51%, respectively. Although the argillaceous tuff core does not have as well-developed fractures as the vitric tuff, it still possesses good pore-throat connectivity. As a result, the utilization degree for small, medium, and large pores is slightly lower than that of the vitric tuff core, reaching 32.21%, 24.13%, and 66.11%, respectively. On the other hand, the argillaceous sandstone core, due to severe capillary retention phenomena, is unable to effectively play the role of the displacement–imbibition coupling effects, especially hindering the effective imbibition between the injected water and the matrix. This leads to low pore-throat utilization degree in small, medium, and large pores, with values of

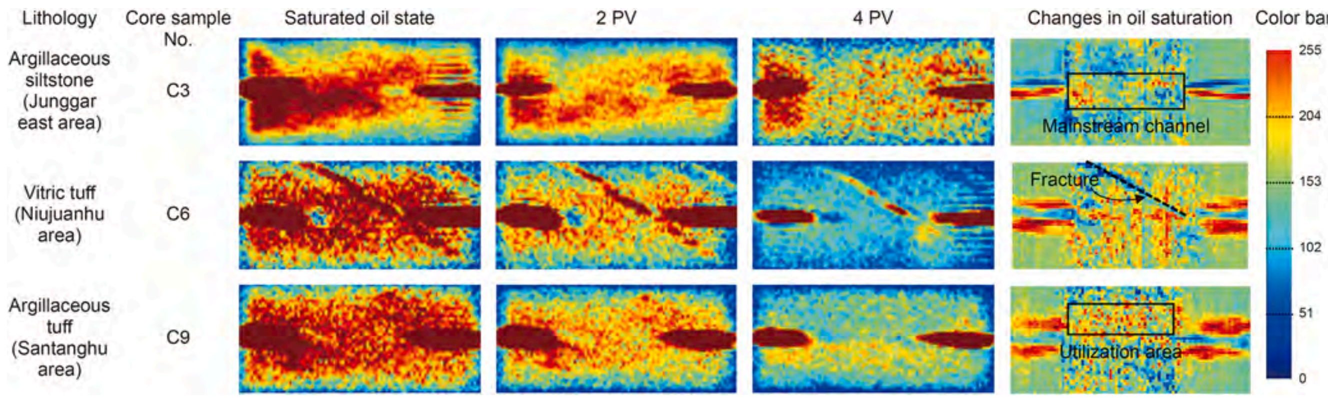

Fig. 18. Distribution and changes in oil saturation at different stages of displacement–imbibition coupling production for cores of different lithologies.

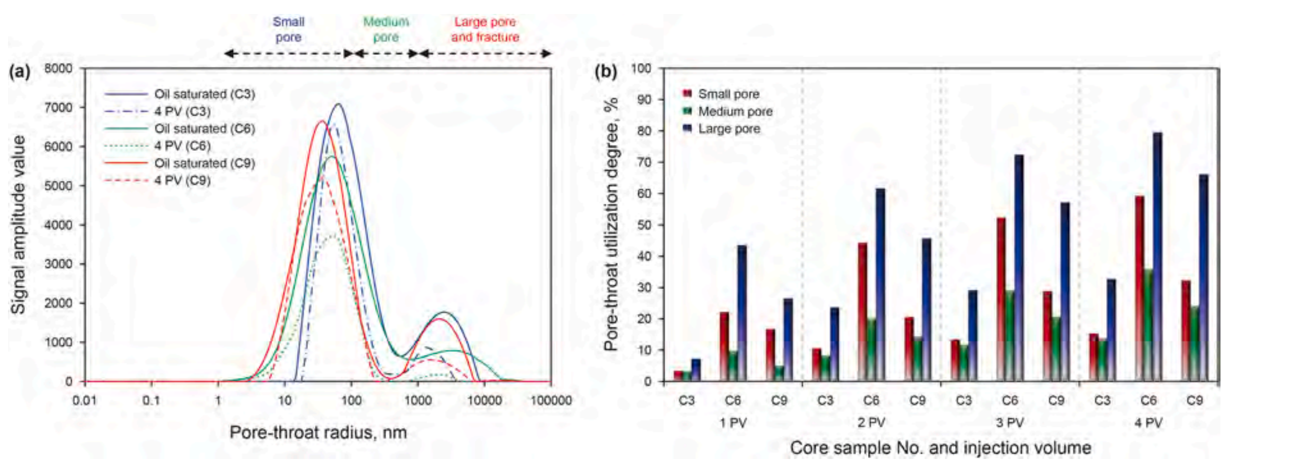

Fig. 19. Effect of lithology. (**a**) NMR T_2 spectral evolution before and after the displacement–imbibition coupling production. (**b**) The relationship between pore-throat utilization and injection volume during the displacement–imbibition coupling production.

15.35%, 13.79%, and 32.72%, respectively. This suggests that a better pore structure can maximize the effectiveness of displacement–imbibition coupling effects, which is conducive to actual production.

Fig. 20(a) shows the relationship between oil displacement efficiency and the injection volume during the displacement–imbibition coupling production for cores of different lithologies. Fig. 20(b) analyzes the contributions of different forces to the oil displacement efficiency during displacement–imbibition coupling production. Similar to the pore-throat utilization degree, the oil displacement efficiency also exhibits a trend of rapid increase followed by a slower rate. For the argillaceous siltstone core sample C3, due to its inherently dense structure and non-development of fractures, its ultimate oil displacement efficiency reached 11.80% after 4 PV of displacement–imbibition coupling production. Of this, the displacement effect contributes 2.41%, the imbibition effect contributes 8.09%, and the displacement–imbibition coupling effects contribute 1.38%. In comparison, the reservoir represented by argillaceous tuff core sample C9 has a fracture density of 10 fractures per meter, resulting in better pore-throat connectivity. Consequently, the ultimate oil displacement efficiency of argillaceous tuff core sample C9 reaches 22.04%. Displacement and imbibition effects increase by 5.53% and 1.29%, reaching 7.94% and 9.38%, respectively, while the displacement–imbibition coupling effects increase oil displacement efficiency by nearly three percentage points, reaching 4.72%. The reservoir represented by vitric tuff core C6 exhibits highly developed fractures, with a fracture density of 33 fractures per meter, resulting in excellent permeability. Its oil displacement efficiency rises rapidly before 2 PV, gradually increasing thereafter. After 4 PV, the contributions of displacement effect, imbibition effect, and displacement–imbibition coupling effects to oil displacement efficiency in small, medium, and large pores are 10.16%, 20.18%, and 7.35%, respectively, resulting in the ultimate oil displacement efficiency of 37.69%. However, due to differences in time scales, boundary conditions, and core-to-reservoir scaling, the overall contribution of imbibition to oil displacement efficiency is typically low in the field, generally less than 1%–2%. Therefore, the experimental results are primarily intended to reveal the microscopic fluid migration mechanisms rather than directly predict field-scale oil production.

These findings highlight that the effectiveness of displacement–imbibition coupling production is governed by the physical properties of lithology and the underlying microscopic mechanisms. Under identical wettability conditions, poor pore-throat connectivity leads to smaller capillary radii, a stronger Jamin effect, and higher flow resistance. However, enhanced capillary forces can extend the reach of imbibition, activating oil recovery over longer distances. Furthermore, factors such as the viscous force at pore walls, the initial pressure gradient required to utilize oil, and interactions between oil and water in confined pores are all strongly influenced by lithological characteristics. Thus, favorable pore-throat structures facilitate the full potential of displacement–imbibition coupling production, reducing resistance to oil–water exchange across pores of various sizes, and thereby improving overall

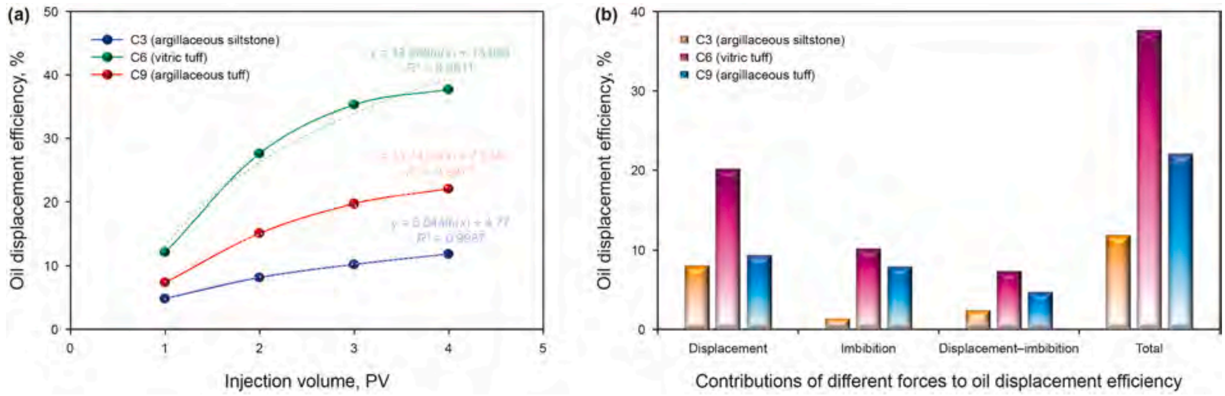

Fig. 20. Effect of lithology. (**a**) Oil displacement efficiency versus injection volume during the displacement–imbibition coupling production. (**b**) Contributions of different forces to oil displacement efficiency during the displacement–imbibition coupling production.

displacement efficiency. Consequently, when designing development strategies, it is critical to first characterize the lithology and pore-throat structure of the target area to enable effective utilization of oil in pores of all sizes.

3.3.2. Effect of fracture penetration ratio

Currently, horizontal well volumetric fracturing in tight and shale oil reservoirs has generated a large number of artificial fractures, which, together with natural fractures, constitute a complex fracture network and improve the storage capacity between the matrix and fractures. This significantly enhances oil flow within the reservoir, making it a critical factor in achieving effective production from tight/shale oil reservoirs. To investigate the effects of fracture penetration ratio and fracture morphology on displacement–imbibition coupling production, we selected argillaceous tuff cores with favorable pore-throat structures from the Santanghu area. Fig. 21 illustrates the distribution and changes in oil saturation before and after displacement–imbibition coupling production with different fracture penetration ratios. As the fracture penetration ratio increases from 0.4 to 0.6, the contact area between fractures and the matrix improves, enhancing the displacement–imbibition coupling effects. This facilitates oil exchange between the fluid and matrix pore spaces, leading to a more pronounced decrease in overall saturation. However, when the fracture penetration ratio reaches 0.8, oil exchange around the left-end fracture is more frequent, leaving minimal residual oil, while in the matrix region near the right-end fracture, less residual oil is observed near the fracture but more at a distance from it. The study indicates that fractures can effectively expand fluid flow within the matrix pore space. However, due to limited utilization distances, simple fracture systems cannot fully displace oil within the matrix. Therefore, complex fracture morphologies are more advantageous in leveraging displacement–imbibition coupling effects, ultimately improving oil displacement efficiency.

Fig. 22(a) illustrates the evolution of NMR T_2 spectra before and after displacement–imbibition coupling production for cores with different fracture penetration ratios. In the initial oil-saturated state, an increase in fracture penetration ratio leads to an enhanced T_2 signal for large pores and fractures, indicating that fractures effectively improve the flow capacity of the matrix. After 4 PV of displacement–imbibition coupling production, the T_2 signal of core sample C10 with a fracture penetration ratio of 0.6 shows a significant decrease, particularly in large pores and fractures, indicating higher oil production from these regions. Simultaneously, the T_2 spectrum reductions for small and medium pores in core sample C10 are the most substantial among the three cores, whereas core sample C11 retains higher T_2 signal values for small and medium pores, suggesting the presence of a considerable amount of residual oil in the matrix pores. Fig. 22(b) presents the relationship between pore-throat utilization and injection volume for core samples C9, C10, and C11 during displacement–imbibition coupling production. All cores exhibit a growth trend that is initially rapid and then slows down. However, increasing the fracture penetration ratio does not consistently translate to higher utilization of different pore sizes. Compared to core sample C9 with a fracture penetration ratio of 0.4, after 4 PV of displacement–imbibition coupling production, core sample C10 (fracture penetration ratio of 0.6) shows increases in utilization of

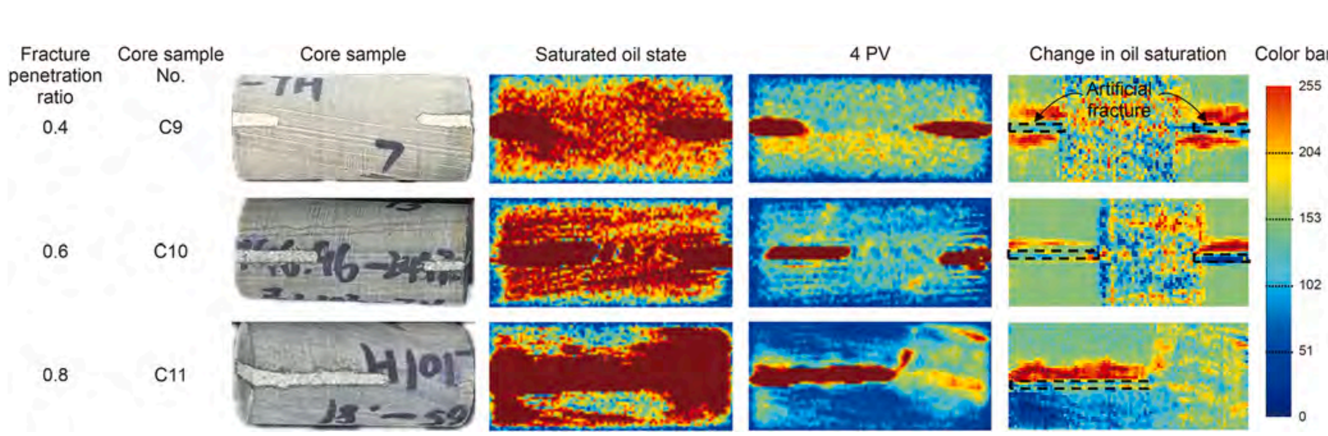

Fig. 21. Distribution and changes in oil saturation before and after displacement–imbibition coupling production with different fracture penetration ratios.

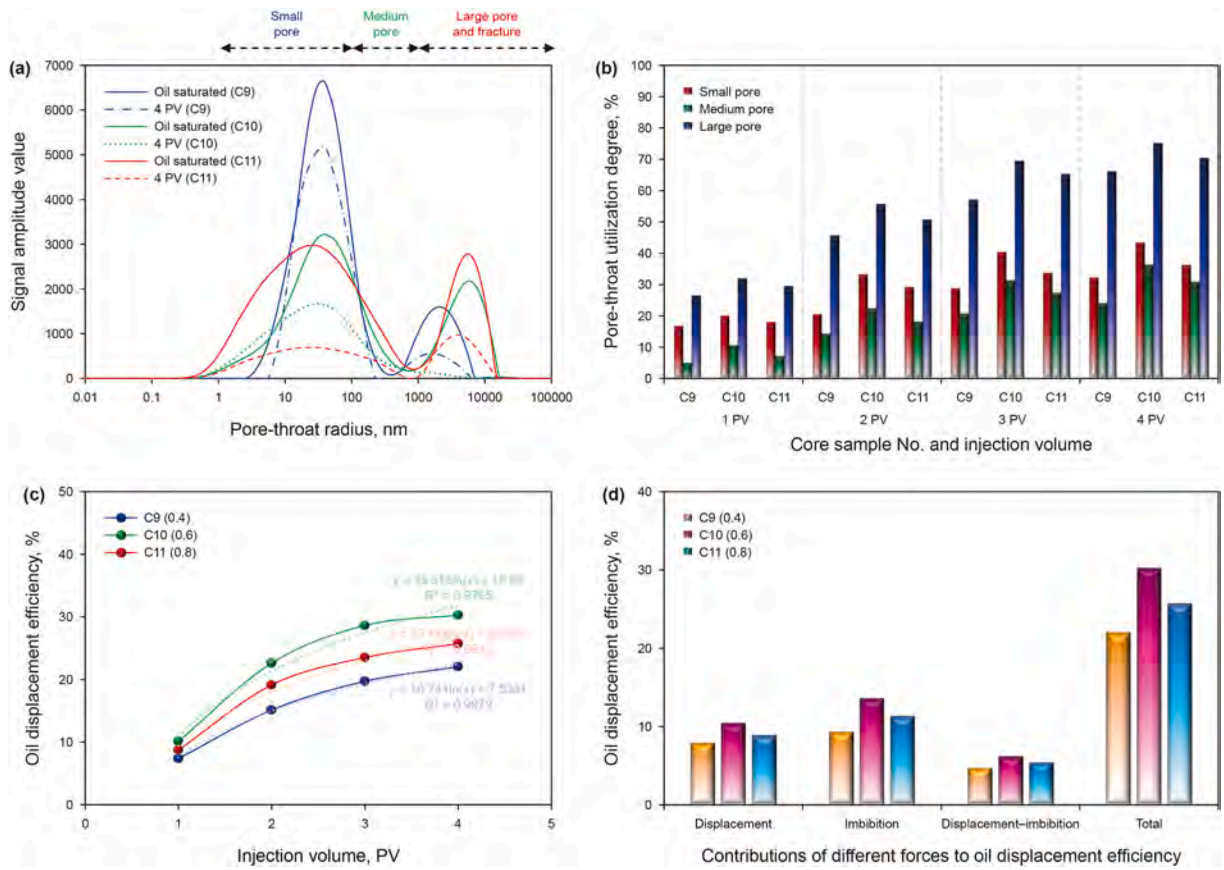

Fig. 22. Effect of fracture penetration ratio. (**a**) NMR T_2 spectral evolution before and after the displacement–imbibition coupling production. (**b**) The relationship between pore-throat utilization and injection volume during the displacement–imbibition coupling production. (**c**) Oil displacement efficiency versus injection volume during the displacement–imbibition coupling production. (**d**) Contributions of different forces to oil displacement efficiency during the displacement–imbibition coupling production.

small, medium, and large pores by 11.19%, 12.18%, and 9.16%, respectively, achieving utilization degrees of 43.41%, 36.32%, and 75.27%, with a total oil displacement efficiency of 30.28% (Fig. 22(c)). In contrast, for core sample C11 (fracture penetration ratio of 0.8), utilization of small, medium, and large pores decreases by 7.13%, 5.47%, and 4.86%, respectively, with a total oil displacement efficiency of 25.73%. This demonstrates that fracture penetration ratio primarily impacts the contact area between the matrix and fractures, influencing oil–fluid exchange in small pores. This effect enhances imbibition contributions, which increased by 4.22% for core sample C10 (Fig. 22(d)). Therefore, in hydraulic fracturing design, it is critical to maintain the fracture penetration ratio at a moderately high level without excessive values to ensure effective utilization of tight and shale reservoirs.

3.3.3. Effect of fracture morphology

Fig. 23 illustrates the oil saturation distribution and changes in cores with different fracture morphologies. Results indicate that core sample C9 exhibits balanced utilization primarily along the mainstream channels, with less residual oil around the two ends of the fractures and accumulation outside the mainstream channels. Core sample C12 is unique, featuring a naturally through-going fracture that spans the entire core. While the fracture increases the contact area between the matrix and the fracture, it also introduces the risk of water channeling. Before a water breakthrough, fluid exchange occurs between the matrix pores and the surrounding fracture. However, when the injected water channels through the fracture, fluid exchange with matrix pores far from the fracture becomes difficult, leading to a significant amount of residual oil near the fracture. In contrast, core sample C13, with a complex matrix–fracture contact relationship, allows the displacement–imbibition coupling effects to be fully utilized at the matrix–fracture interface and within the matrix pores before water channeling. However, once a channeling pathway forms, fluid rapidly flows through the preferential water drive channels, bypassing matrix pores and leaving some residual oil far from the fracture. Nevertheless, the complex fracture network in core sample C13 enables extensive utilization of most pore spaces.

Fig. 24(a) illustrates the evolution of the NMR T_2 spectra during the displacement–imbibition coupling production for cores with different fracture morphologies. The spectra reveal a bimodal distribution dominated by nanoscale small pores and microscale large pores, with some partially developed intermediate-sized pores. By analyzing the T_2 spectra before and after displacement, it is evident that with increasing injection volume, the T_2 spectrum for small pores shifts to the right, accompanied by a gradual decrease in signal intensity and movement toward larger relaxation times. This trend indicates that oil in the small matrix pores progressively migrates to larger pores under the displacement–imbibition coupling effects. Both cocurrent imbibition and counter-current imbibition occur simultaneously across different pore sizes, driving the continuous transfer of oil from small matrix pores through intermediate and large pores to fractures. Fig. 24(b) and (c) depict the pore-throat utilization degree and oil displacement efficiency as a function of injection volume during the displacement–imbibition coupling production for cores with different fracture morphologies. All cores demonstrate a rapid increase in the early stages, followed by a slower growth trend, with cores exhibiting more complex fracture morphology achieving higher overall growth. After 4 PV of displacement–imbibition

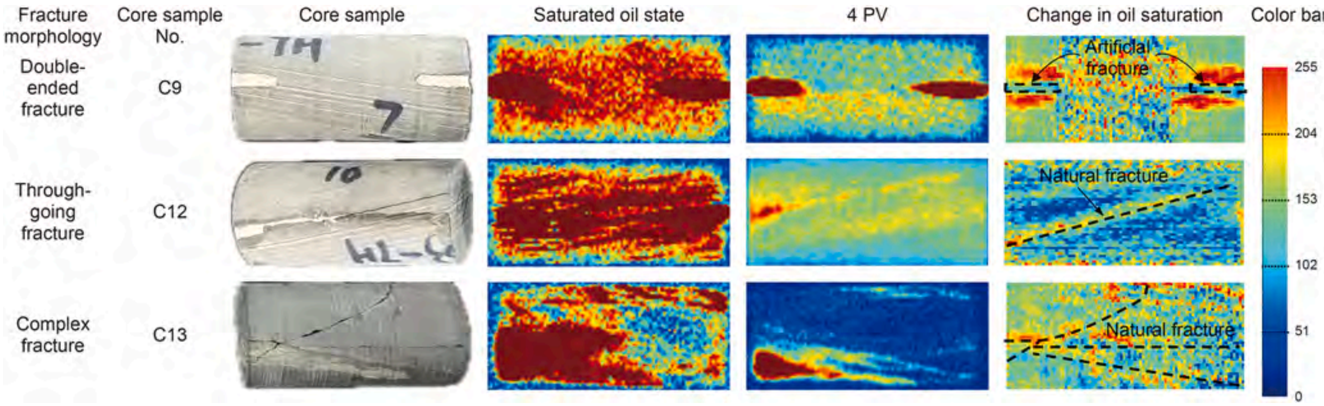

Fig. 23. Distribution and changes in oil saturation before and after displacement–imbibition coupling production for cores with different fracture morphologies.

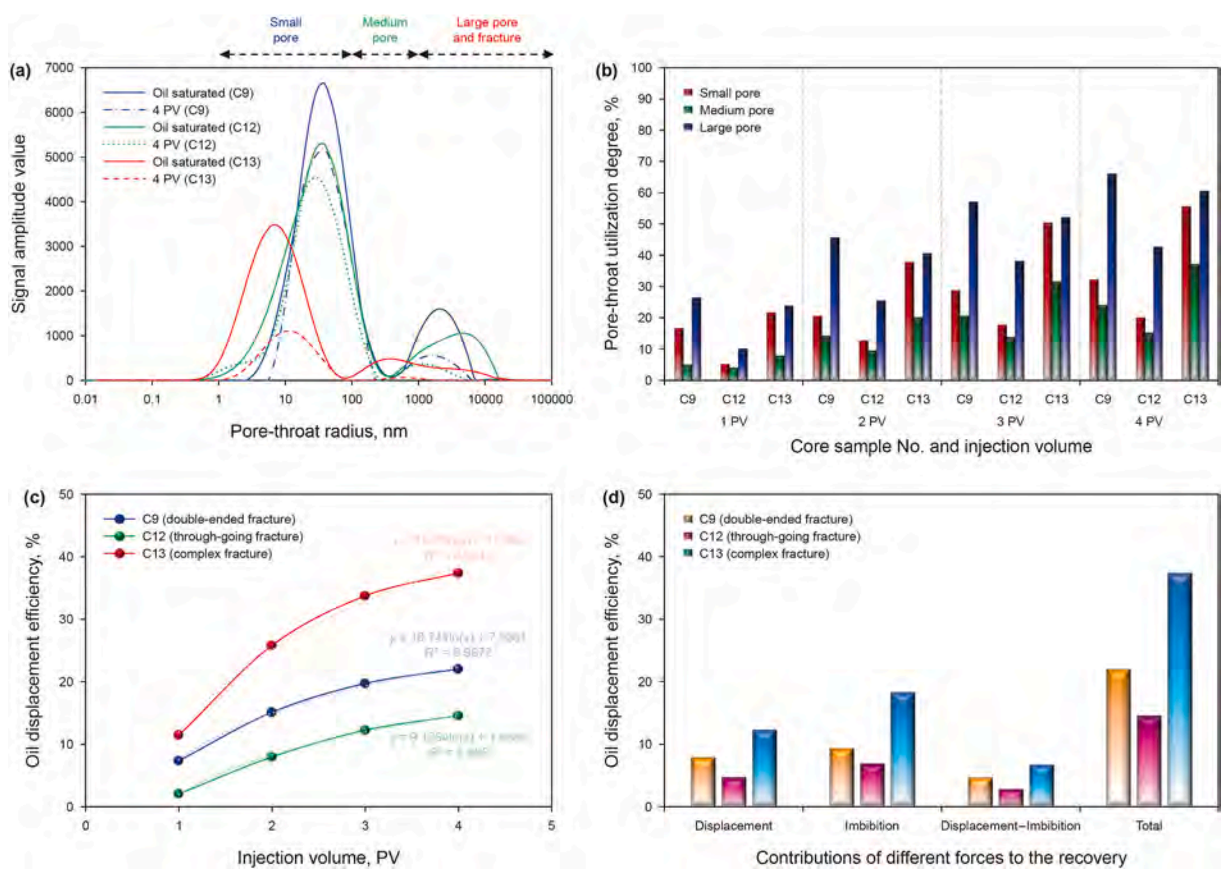

Fig. 24. Effect of fracture morphology. (**a**) NMR T_2 spectral evolution before and after the displacement–imbibition coupling production. (**b**) The relationship between pore-throat utilization and injection volume during the displacement–imbibition coupling production. (**c**) Oil displacement efficiency versus injection volume during the displacement–imbibition coupling production. (**d**) Contributions of different forces to oil displacement efficiency during the displacement–imbibition coupling production.

coupling production, the ultimate displacement efficiencies for core samples C9, C12, and C13 are 22.04%, 14.57%, and 37.39%, respectively. Compared to the core C9 with double-ended fracture, the core sample C12, influenced by a through-fracture, shows lower oil displacement efficiency and pore-throat utilization across different pore sizes. The utilization degrees for small, medium, and large pores are 20.17%, 15.32%, and 42.68%, respectively. Conversely, the core sample C13 with complex fractures exhibits significant improvements in the utilization degrees of small and medium pores, reaching 55.63% and 37.21%, respectively, although the utilization degree of large pores slightly declines by 5.58%–60.53%. This suggests that increasing fracture complexity enhances the contact area between the matrix and fractures, thereby strengthening capillary imbibition, particularly in fracture-dense regions. Consequently, the utilization degrees of small and medium pores increase significantly. However, the enhanced capillary imbibition can reduce the dominance of displacement mechanisms, leading to a slight decline in the utilization degree of large pores and fractures.

An analysis of the contributions of different driving forces to oil displacement efficiency (Fig. 24(d)) shows that complex fracture morphology significantly enhances reservoir permeability, improving the effects of displacement, imbibition, and their coupling. This results in a notable increase in ultimate displacement efficiency. However, the risk of water channeling associated with fractures cannot be ignored. For instance, the contributions of all driving forces to displacement efficiency in the core sample C12 are lower compared to the core sample C9, due to the adverse effects of water channeling. In summary, fractures play a critical role in increasing the contact area between the matrix and fluids, reducing oil–water flow resistance, and facilitating fluid exchange between the matrix and fractures, thereby enhancing oil displacement efficiency. However, careful attention must be given to the risk of water channeling induced by fractures during reservoir development.

Additionally, before conducting the oil–water two-phase displacement–imbibition experiment, a water flooding test was performed on the core sample C9 to record the pressure gradient at different flow rates, thereby obtaining the flow rate–pressure gradient curve for the core sample C9, as shown in Fig. 25. Several critical points are identified during the experiment: Point A represents the absolute starting pressure gradient (G_p), corresponding to the pressure gradient required for fluid flow through the largest pore channels in the medium. Point B is the quasi-starting pressure gradient (G_c), which reflects the starting pressure gradient for fluid flow through the average pore diameter channels. Point C marks the transition between nonlinear and linear flow, indicating the critical pressure gradient for this transition. Point D denotes the minimum flow rate of the pump. Point E is the transition point between the linear and nonlinear flow segments. Based on these critical points and the complexity of fluid flow, the concept of nonlinear flow zoning is proposed to characterize fluid flow in tight and shale reservoirs. In the linear flow region fluid flow is dominated by linear flow, and both large and small pores in the matrix can be utilized. In the nonlinear flow region, fluid flow is dominated by nonlinear flow, with large pores in the matrix being utilized while small pores are not utilized. In the strongly nonlinear flow region, the heterogeneity is more pronounced, with nonlinear flow dominating, and both large and small pores in the matrix are difficult to utilize. Therefore, to avoid water breakthrough while maximizing the effect of the displacement–imbibition coupling production, the following two aspects should be considered: (1) Ensure that the pressure gradient during the injection stage exceeds the minimum pressure gradient of the strongly nonlinear flow region, which corresponds to the minimum stable liquid production rate. This ensures that

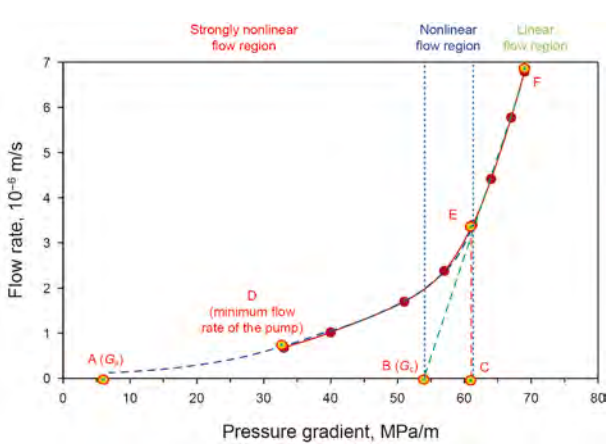

Fig. 25. Flow rate versus pressure gradient curve and nonlinear flow zoning diagram of core sample C9.

the displacement effect can overcome the capillary forces between the pore-throat, allowing injected water to effectively enter the pores of different sizes for fluid exchange. (2) Ensure that the pressure gradient during the injection stage is lower than the maximum pressure gradient of the linear flow region, which corresponds to the maximum stable liquid production rate. This prevents water breakthrough and maximizes the displacement–imbibition coupling effects. When conducting large-scale volume fracturing in field applications, it is important to avoid connecting artificial fractures between wells while ensuring sufficient contact between the artificial fractures and the reservoir matrix. Multiple rounds of displacement–imbibition coupling production should be utilized to extract more oil from the matrix and fractures, thereby improving the recovery rate.

4. Discussion

As demonstrated by the results of the real-time NMR displacement–imbibition coupling production experiments and the nonlinear flow zoning concept, the displacement–imbibition process in tight/shale oil reservoirs involves fluid flow across different flow regions. These are classified into three flow modes: flow in linear flow region with well-connected pores and complex fracture networks, flow in nonlinear flow region using large pores and partial artificial fractures as displacement–imbibition pathways, and flow in strongly nonlinear flow region dominated by small pores and natural fractures. Therefore, this study proposes a oil–water two-phase displacement–imbibition flow model for tight and shale reservoirs based on the nonlinear flow zoning concept, integrating artificial fractures, natural fractures, and matrix (Fig. 26). During displacement–imbibition coupling production in tight and shale reservoirs, artificial fractures created by hydraulic fracturing connect with natural fractures in the linear flow region to form a complex fracture network. At this stage, oil from matrix pores is produced through the fracture network formed by volumetric fracturing. As production from the fracture network declines, oil in the matrix pores of the nonlinear flow region migrates to large pores and artificial fractures. However, due to the limited capacity of artificial fractures, flow in this region mainly involves utilizing oil from large pores. The strongly nonlinear flow region, which contains the most oil but is the hardest to develop, features matrix pores with high flow resistance and capillary forces. By leveraging displacement–imbibition coupling effects and natural fractures, effective utilization in this region can be achieved, enabling oil to migrate from pores to the wellbore. Natural fractures serve as bridges connecting the matrix and artificial fractures, significantly enhancing fluid flow within the porous medium. Reservoirs with well-developed natural fractures are more likely to form complex fracture networks, converting the pores in strongly nonlinear flow regions to those in nonlinear flow regions or even linear flow regions. This reduces flow resistance, utilizes residual oil, and facilitates oil migration to the wellbore for production. Thus, large-scale volumetric fracturing can significantly enhance the utilization of pores in the near-wellbore region, particularly in the linear and nonlinear flow regions. However, for strongly nonlinear flow regions, additional strategies such as reduced well spacing and displacement–imbibition coupling oil production are required to increase the inter-well pressure gradient, thereby optimizing fluid flow and achieving EOR. In the near future, we will consider the influencing factors of nonlinear flow zoning at each stage of injection, shut in, and production, as well as EOR optimization, to explore more efficient development methods for tight/shale oil reservoirs.

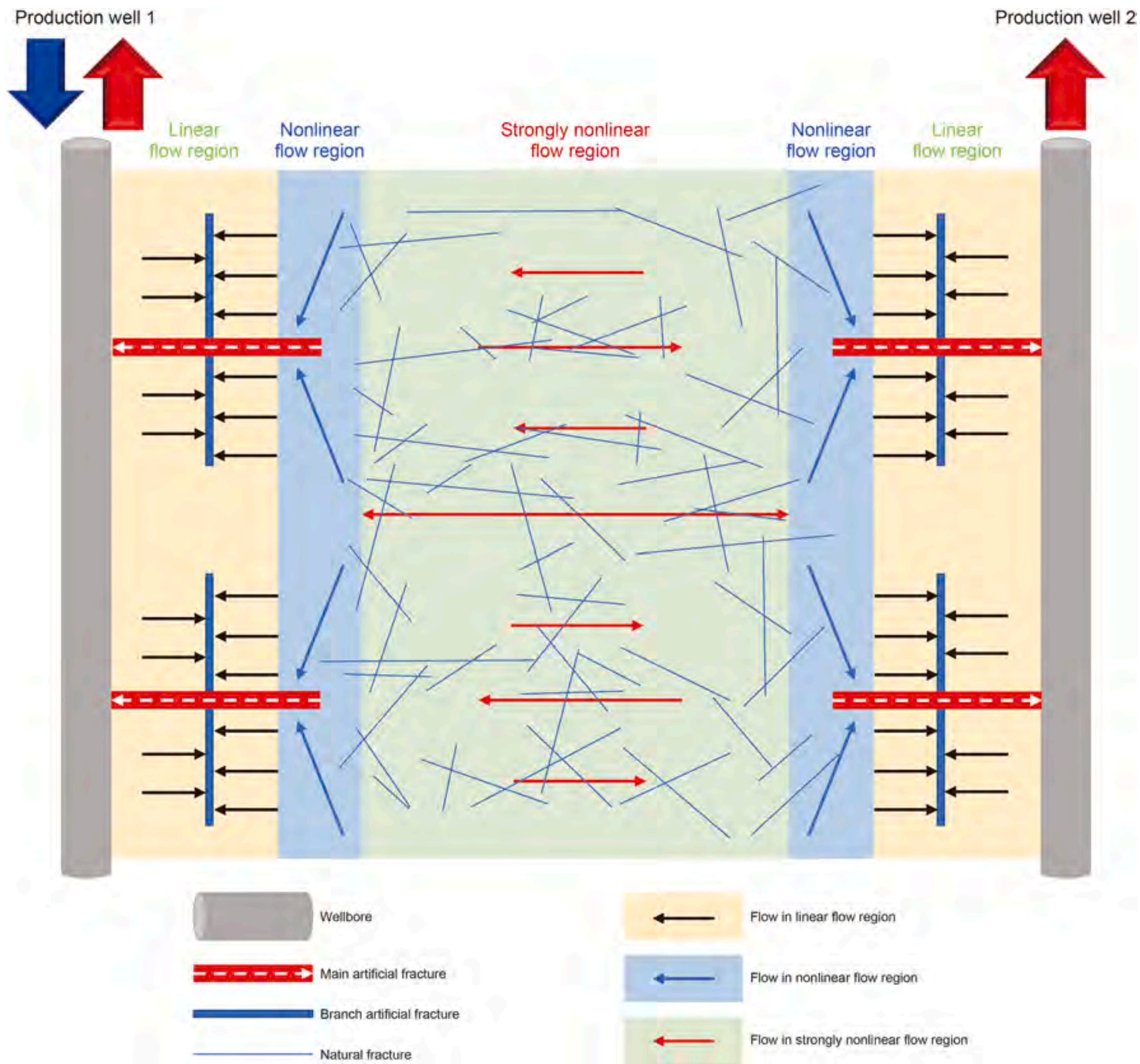

Fig. 26. The oil–water two-phase displacement–imbibition flow model of matrix and fracture for tight and shale reservoirs based on the nonlinear flow zoning concept.

5. Conclusions

In this study, a series of online NMR oil–water two-phase displacement–imbibition experiments are conducted, focusing on the displacement–imbibition coupling mechanism between the matrix and fractures. Additionally, a new characterization method for oil saturation in different regions based on image processing is proposed. The dynamic evolution of various lithologies, injection strategies, and fracture complexities is monitored, providing insight into the pore-scale displacement mechanisms of oil under diverse influencing factors. Furthermore, the extent of pore-throat utilization across different pore sizes under various influencing factors and the contribution of distinct driving forces to oil displacement efficiency are quantified. The main research conclusions are as follows.

(1) In tight/shale oil reservoirs, there are two main driving forces for crude oil displacement in the reservoir pores: displacement effect occurs primarily in large pores and fractures, while imbibition effect mainly occurs in medium and small pores. Both continuous injection (dominated by displacement effect) and water huff and puff (dominated by imbibition effect) have limitations by only utilizing the dominant pores. However, displacement–imbibition coupling production with its multi-drive forces (displacement–imbibition coupling effects), effectively achieves balanced utilization of pores of different sizes, making it an excellent method for improving oil recovery.

(2) The displacement–imbibition oil production mainly consists of three stages: the water injection stage dominated by displacement effect, the shut-in stage dominated by capillary imbibition, and the production stage of displacement–imbibition coupling effects. Artificially altering the pressure field of the matrix pores creates pressure oscillations between the pores, effectively enhancing or releasing capillary imbibition and reducing the pore-throat utilization threshold, which is key to the displacement–imbibition coupling production.

(3) The reservoir lithology determines the ease of displacement–imbibition oil production. Lithologies with stronger heterogeneity and better pore-throat connectivity can reduce the resistance to oil–water flow through the pores, facilitating the effective implementation of displacement–imbibition coupling effects and enhancing the utilization of pores of different sizes. The ultimate oil displacement efficiency of vitric tuff with better pore-throat

structure is 37.69%, which is 25.89% higher than that of the ultimate oil displacement efficiency of the argillaceous siltstone.

(4) The complexity of the matrix and fractures significantly affects fluid exchange during the displacement–imbibition oil production, with fracture penetration ratio and fracture morphology being two key factors. The more complex the contact relationship between the matrix and fractures, the easier it is for oil droplets to be displaced from the pore spaces with larger contact areas between the fluid and the matrix. The capillary imbibition between the matrix and fractures is enhanced, while the displacement effect is weakened. To maximize the effectiveness of displacement–imbibition coupling production while avoiding water channeling, effectively utilizing fractures is crucial.

(5) It should be noted that the core length used in this study was limited by the NMR/MRI equipment, which may restrict the full development of capillary-driven imbibition fronts and underestimate long-distance matrix–fracture interactions. In addition, water-phase permeability was estimated from air permeability using an empirical formula, which may introduce uncertainty in comparative analysis. These limitations have been acknowledged, and future work should explore longer cores and direct permeability measurements to improve accuracy and applicability.

CRediT authorship contribution statement

Bin-Yu Wang: Writing – original draft, Methodology, Conceptualization. **Ren-Yi Cao:** Supervision, Investigation, Funding acquisition. **Xin-Yi Zheng:** Methodology, Investigation. **Lin-Song Cheng:** Investigation, Funding acquisition. **Jiang-Peng Hu:** Methodology, Conceptualization. **Zhi-Hao Jia:** Validation, Data curation. **Wen-Hao Duan:** Investigation. **Hassan Hassanzadeh:** Writing – review & editing.

Declaration of competing interest

We declare that we have no financial and personal relationships with other people or organizations that can inappropriately influence our work, there is no professional or other personal interest of any nature or kind in any production, service and or company that could be construed as influencing the position presented in, or the manuscript entitled.

Acknowledgments

We acknowledge that this study was partially supported by the National Natural Science Foundation of China (No. 52174038) and the Science Foundation of China University of Petroleum, Beijing (No. 2462018YJRC015). In addition, the support of the Department of Chemical and Petroleum Engineering of University of Calgary and the China Scholarship Council (No. 202406440057) is highly appreciated.

References

Cai, J.-C., Chen, Y., Qiao, J.-C., Yang, L., Zeng, J.-H., Sun, C.-H., 2022. Determination of dynamic capillary effect on two-phase flow in porous media: A perspective from various methods. Pet. Sci. 19 (4), 1641–1652. https://doi.org/10.1016/j.petsci.2022.01.017.

Cheng, Y., Di, Q., Gu, C., Ye, F., Hua, S., Yang, P., 2015. Visualization study on fluid distribution and end effects in core flow experiments with low-field mri method. J. Hydrodyn. 27 (2), 187–194. https://doi.org/10.1016/S1001-6058(15)60471-1.

Dai, C., Cheng, R., Sun, X., Liu, Y., Zhou, H., Wu, Y., You, Q., Zhang, Y., Sun, Y., 2019. Oil migration in nanometer to micrometer sized pores of tight oil sandstone during dynamic surfactant imbibition with online NMR. Fuel 245, 544–553. https://doi.org/10.1016/j.fuel.2019.01.021.

Dou, L., Xiao, Y., Gao, H., Wang, R., Liu, C., Sun, H., 2021. The study of enhanced displacement efficiency in tight sandstone from the combination of spontaneous and dynamic imbibition. J. Petrol. Sci. Eng. 199, 108327. https://doi.org/10.1016/j.petrol.2020.108327.

Du, M., Zhengming, Y., Lv, W., Xiao, Q., Xiang, Q., Yao, L., Feng, C., 2024. Experimental study on microscopic production characteristics and influencing factors during dynamic imbibition of shale reservoir with online NMR and fractal theory. Energy 310, 133244. https://doi.org/10.1016/j.energy.2024.133244.

EIA, 2022. Drilling Productivity Report: For Key Tight Oil and Shale Gas Regions. EIA Independent Statistics & Analysis, Washington.

Fu, C., Xu, X., Du, Y., Kou, X., 2024. Experimental study on the influence of pore structure on spontaneous imbibition in marine black shale. Capillarity 10 (3), 57–72. https://doi.org/10.46690/capi.2024.03.01.

Ghandi, E., Parsaei, R., Riazi, M., 2019. Enhancing the spontaneous imbibition rate of water in oil-wet dolomite rocks through boosting a wettability alteration process using carbonated smart brines. Pet. Sci. 16 (6), 1361–1373. https://doi.org/10.1007/s12182-019-0355-1.

Guo, X., Semnani, A., Ekekeh, D.G., Gao, Z., Ostadhassan, M., Jia, H., Fu, J., Ying, W., 2021. Experimental study of spontaneous imbibition for oil recovery in tight sandstone cores under high pressure high temperature with low field nuclear magnetic resonance. J. Petrol. Sci. Eng. 201, 108366. https://doi.org/10.1016/j.petrol.2021.108366.

Han, X., Yu, H., Tang, H., Song, P., Huang, T., Liu, C., Wang, Y., 2024. Investigation on oil recovery and countercurrent imbibition distance coupling carbonated water with surfactant in shale oil reservoirs. Fuel 374, 132409. https://doi.org/10.1016/j.fuel.2024.132409.

Harimi, B., Masihi, M., Mirzaei-Paiaman, A., Hamidpour, E., 2019. Experimental study of dynamic imbibition during water flooding of naturally fractured reservoirs. J. Petrol. Sci. Eng. 174, 1–13. https://doi.org/10.1016/j.petrol.2018.11.008.

Jia, Z., Cheng, L., Feng, H., Cao, R., Jia, P., Pu, B., Pan, Q., Shi, J., 2023. Full composition numerical simulation of CO_2 utilization process in shale reservoir using projection-based embedded discrete fracture model (pEDFM) considering nano-confinement effect. Gas Sci. Eng. 111, 204932. https://doi.org/10.1016/j.jgsce.2023.204932.

Jiang, J., Rui, Z., Hazlett, R., Lu, J., 2019. An integrated technical-economic model for evaluating CO_2 enhanced oil recovery development. Appl. Energy 247, 190–211. https://doi.org/10.1016/j.apenergy.2019.04.025.

Jiang, T., Shen, Z., Wang, L., Qi, Z., Xiao, B., Qin, Q., Fan, X., Wang, Y., Qu, H., 2024. Optimization method of fracturing fluid volume intensity for SRV fracturing technique in shale oil reservoir based on forced imbibition: A case study of well X-1 in Biyang Sag of Nanxiang Basin, China. Petrol. Explor. Dev. 51 (3), 674–683. https://doi.org/10.1016/S1876-3804(24)60496-9.

Jiang, Z., Li, G., Zhao, P., Zhou, Y., Mao, Z., Liu, Z., 2023. Study on spontaneous imbibition and displacement characteristics of mixed-wet tight sandstone reservoir based on high-precision balance and NMR method. Fuel 345, 128247. https://doi.org/10.1016/j.fuel.2023.128247.

Jin, Z., Zhu, R., Liang, X., Shen, Y., 2021. Several issues worthy of attention in current lacustrine shale oil exploration and development. Petrol. Explor. Dev. 48 (6), 1471–1484. https://doi.org/10.1016/S1876-3804(21)60303-8.

Kerunwa, A., Onyekonwu, M.O., Anyadiegwu, C.I., Olafuyi, A.O., 2016. Spontaneous imbibition in Niger Delta cores. In: SPE Nigeria Annual International Conference and Exhibition. https://doi.org/10.2118/184353-MS.

Lei, Q., Xu, Y., Cai, B., Guan, B., Wang, X., Bi, G., Li, H., Li, S., Ding, B., Fu, H., Tong, Z., Li, T., Zhang, H., 2022. Progress and prospects of horizontal well fracturing technology for shale oil and gas reservoirs. Petrol. Explor. Dev. 49 (1), 191–199. https://doi.org/10.1016/S1876-3804(22)60015-6.

Lei, Z., Wang, Z., Mu, L., Peng, H., Li, X., Bai, X., Tao, Z., Li, H., Peng, Y., 2024. A technique for enhancing tight oil recovery by multi-field reconstruction and combined displacement and imbibition. Petrol. Explor. Dev. 51 (1), 152–163. https://doi.org/10.1016/S1876-3804(24)60012-1.

Li, C., Shen, Y., Ge, H., Zhang, Y., Liu, T., 2018. Spontaneous imbibition in fractal tortuous micro-nano pores considering dynamic contact angle and slip effect: Phase portrait analysis and analytical solutions. Sci. Rep. 8 (1), 3919. https://doi.org/10.1038/s41598-018-21002-y.

Li, S., Ye, Z., Wang, J., Tang, L., Lai, N., 2023. Effects of fracturing fluid composition and other factors on improving the oil imbibition recovery of shale reservoir. Capillarity 9 (3), 45–54. https://doi.org/10.46690/capi.2023.12.01.

Lin, M., Wang, P., Li, Q., 2016. Analysis of the effect of different throughput methods of Chang 7 tight oil horizontal wells in an 83 district. Petrochem. Indus. Appl. 35 (6), 94–97 (in Chinese).

Liu, C., You, Q., Wang, T., Zhou, B., Peng, W., Du, Y., Liu, Y., Li, Y., Dai, C., 2024. Study of microscopic imbibition and formation plugging mechanism of the compact oil reservoir based on SEM and NMR analysis. Fuel 357, 129672. https://doi.org/10.1016/j.fuel.2023.129672.

Lu, M., Qian, Q., Zhong, A., Zhang, Z., Zhang, L., 2024. Investigation on the flow behavior and mechanisms of water flooding and CO_2 immiscible/miscible flooding in shale oil reservoirs. J. CO_2 Util. 80, 102660. https://doi.org/10.1016/j.jcou.2023.102660.

Lv, W., Chen, S., Gao, Y., Kong, C., Jia, N., He, L., Wang, R., Li, J., 2019. Evaluating seepage radius of tight oil reservoir using digital core modeling approach. J. Petrol. Sci. Eng. 178, 609–615. https://doi.org/10.1016/j.petrol.2019.03.072.
Meng, Q., Zhao, L., Li, P., Yang, F., Cai, J., 2022. Experiments and phase-field simulation of counter-current imbibition in porous media with different pore structure. J. Hydrol. 608, 127670. https://doi.org/10.1016/j.jhydrol.2022.127670.
Peng, Y., Wang, Y., Lei, Z., Wang, X., Wang, D., Zhang, G., Zhou, D., 2024. Investigation on availability of method combining waterflooding and soaking for tight oil reservoirs. Sci. Technol. Eng. 24 (4), 1448–1458 (in Chinese).
Qu, Z., Wang, J., Guo, T., Shen, L., Liao, H., Liu, X., Fan, J., Hao, T., 2021. Optimization on fracturing fluid flowback model after hydraulic fracturing in oil well. J. Petrol. Sci. Eng. 204, 108703. https://doi.org/10.1016/j.petrol.2021.108703.
Ren, W., Ma, C., Huang, X., Gu, W., Chen, Y., Liu, X., 2023. Dynamic and static imbibition characteristics of tight sandstone based on NMR. Geoenergy Sci. Eng. 229, 212052. https://doi.org/10.1016/j.geoen.2023.212052.
Sheng, J.J., Chen, K., 2014. Evaluation of the EOR potential of gas and water injection in shale oil reservoirs. J. Unconv. Oil Gas Res. 5, 1–9. https://doi.org/10.1016/j.juogr.2013.12.001.
Song, Y., Song, Z., Meng, Y., Chen, Z., Han, X., Feng, D., 2024. Multi-phase behavior and pore-scale flow in medium-high maturity continental shale reservoirs with oil, CO_2, and water. Chem. Eng. J. 484, 149679. https://doi.org/10.1016/j.cej.2024.149679.
Syed, F.I., Dahaghi, A.K., Muther, T., 2022. Laboratory to field scale assessment for EOR applicability in tight oil reservoirs. Pet. Sci. 19 (5), 2131–2149. https://doi.org/10.1016/j.petsci.2022.04.014.
Takahashi, S., Kovscek, A.R., 2010. Spontaneous countercurrent imbibition and forced displacement characteristics of low-permeability, siliceous shale rocks. J. Petrol. Sci. Eng. 71 (1–2), 47–55. https://doi.org/10.1016/j.petrol.2010.01.003.
Tian, W., Wu, K., Feng, D., Gao, Y., Li, J., Chen, Z., 2023. Dynamic contact angle effect on water-oil imbibition in tight oil reservoirs. Energy 284, 129209. https://doi.org/10.1016/j.energy.2023.129209.
Vilhena, O., Farzaneh, A., Pola, J., March, R., Sisson, A., Sohrabi, M., 2019. Experimental and numerical evaluation of spontaneous imbibition processes in unfractured and fractured carbonate cores with stress-induced apertures. In: SPE Europec Featured at 81st EAGE Conference and Exhibition. https://doi.org/10.2118/195452-MS.
Wang, B., Cao, R., Pi, Z., Cheng, L., Jia, Z., Hu, J., 2024. Displacement-imbibition coupling mechanisms between matrix and complex fracture during injecting-shut in-production process using pore-scale simulation and NMR experiment. Geoenergy Sci. Eng. 242, 213254. https://doi.org/10.1016/j.geoen.2024.213254.
Wang, C., Gao, H., Qi, Y., Li, X., Zhang, R., Fan, H., 2020. Investigation on the mechanisms of spontaneous imbibition at high pressures for tight oil recovery. ACS Omega 5 (22), 12727–12734. https://doi.org/10.1021/acsomega.0c00186.
Wang, X., Wang, M., Li, Y., Zhang, J., Li, M., Li, Z., Guo, Z., Li, J., 2021. Shale pore connectivity and influencing factors based on spontaneous imbibition combined with a nuclear magnetic resonance experiment. Mar. Petrol. Geol. 132, 105239. https://doi.org/10.1016/j.marpetgeo.2021.105239.
Wei, Q., Li, Z., Wang, X., Bai, R., Wang, C., Li, H., 2016. Mechanism and influence factors of imbibition in fractured tight sandstone reservoir: An example from Chang8 reservoir of Wuqi area in Ordos Basin. Petrol. Geol. Recov. Effic. 23 (4), 102–107 (in Chinese).
Wu, Z., Li, L., Yan, Y., 2019. New development pattern of network fracturing and imbibition oil recovery for super-low permeability oil reservoirs. Fault-Block Oil Gas Field 26 (4), 491–494 (in Chinese).
Xiong, Y., Li, S., Li, M., Leng, A., Chen, M., Deng, B., Yu, K., 2025. Study on characteristics of imbibition and recovery predicted methods with different lithology structure. Fuel 381, 133525. https://doi.org/10.1016/j.fuel.2024.133525.
Xu, L., Li, Q., Myers, M., Tan, Y., Chen, Q., Li, X., 2020. Flow behavior characteristics and residual trapping of supercritical carbon dioxide in tight glutenite by MRI experiments. J. Nat. Gas Sci. Eng. 83, 103540. https://doi.org/10.1016/j.jngse.2020.103540.
Yang, L., Ge, H., Shi, X., Cheng, Y., Zhang, K., Chen, H., Shen, Y., Zhang, J., Qu, X., 2016. The effect of microstructure and rock mineralogy on water imbibition characteristics in tight reservoirs. J. Nat. Gas Sci. Eng. 34, 1461–1471. https://doi.org/10.1016/j.jngse.2016.01.002.
Yu, F., Gao, Z., Zhu, W., Wang, C., Liu, F., Xu, F., Jiang, H., Li, J., 2021. Experiments on imbibition mechanisms of fractured reservoirs by microfluidic chips. Petrol. Explor. Dev. 48 (5), 1162–1172. https://doi.org/10.1016/S1876-3804(21)60099-X.
Yuan, Y., Rezaee, R., Zhou, M.-F., Iglauer, S., 2023. A comprehensive review on shale studies with emphasis on nuclear magnetic resonance (NMR) technique. Gas Sci. Eng. 120, 205163. https://doi.org/10.1016/j.jgsce.2023.205163.
Zhang, J., Deng, B., Zhang, H., 2022. Experimental study on static and dynamic imbibition and oil-increasing mechanism of tight sand-stone. Sci. Technol. Eng. 22 (24), 10526–10533.
Zhang, P.-F., Lu, S.-F., Li, J.-Q., Chang, X.-C., Zhang, J.-J., Pang, Y.-M., Lin, Z.-Z., Chen, G., Yin, Y.-J., Liu, Y.-Q., 2023. Quantitative characterization of shale pore connectivity and controlling factors using spontaneous imbibition combined with nuclear magnetic resonance T_2 and T_1-T_2. Pet. Sci. 20 (4), 1947–1960. https://doi.org/10.1016/j.petsci.2023.03.011.
Zhang, Q., Liu, J.-F., Gao, Z.-H., Chen, S.-Y., Liu, B.-Y., 2023. Review on the challenges and strategies in oil and gas industry's transition towards carbon neutrality in China. Pet. Sci. 20 (6), 3931–3944. https://doi.org/10.1016/j.petsci.2023.06.004.
Zhang, Y.-w., Z., Yang, C.-h., 2024. Study on the imbibition production mechanism and main controlling factors of low-permeability reservoir. RSC Adv. 14 (42), 31183–31192. https://doi.org/10.1039/D4RA05036C.
Zhang, Y., Chang, J., Jiang, Z., Gao, Z., Zhang, C., Wang, G., Shao, X., He, W., 2024. Visualization of dynamic micro-migration of shale oil and investigation of shale oil movability by NMRI combined oil charging/water flooding experiments: A novel approach. Mar. Petrol. Geol. 165, 106907. https://doi.org/10.1016/j.marpetgeo.2024.106907.
Zou, C., Ma, F., Pan, S., Zhang, X., Wu, S., Fu, G., Wang, H., Yang, Z., 2023. Formation and distribution potential of global shale oil and the developments of continental shale oil theory and technology in China. Earth Sci. Front. 30 (1), 128–142. https://doi.org/10.13745/j.esf.sf.2022.8.29.